The Astronomical Journal, 164:187 (16pp), 2022 November https://doi.org/10.3847/1538-3881/ac90bc

High-velocity Stars in SDSS/APOGEE DR17

F. Quispe-Huaynasi[1], F. Roig[1], D. J. McDonald[2], V. Loaiza-Tacuri[1], S. R. Majewski[2], F. C. Wanderley[1], K. Cunha[3], C. B. Pereira[1], S. Hasselquist[4], and S. Daflon[1]
[1] Observatorio Nacional, Rio de Janeiro, RJ 20921-400, Brazil; froig@on.br
[2] Department of Astronomy, University of Virginia, Charlottesville, VA 22904, USA
[3] Steward Observatory, University of Arizona, Tucson, AZ 85721, USA
[4] Space Telescope Science Institute, Baltimore, MD 21218, USA
Received 2022 August 15; revised 2022 September 5; accepted 2022 September 7; published 2022 October 12

Abstract

We report 23 stars having Galactocentric velocities larger than 450 km s^{-1} in the final data release of the APOGEE survey. This sample was generated using space velocities derived by complementing the high-quality radial velocities from the APOGEE project in Sloan Digital Sky Survey's Data Release 17 (DR17) with distances and proper motions from Gaia early Data Release 3 (eDR3). We analyze the observed kinematics and derived dynamics of these stars, considering different potential models for the Galaxy. We find that three stars could be unbound depending on the adopted potential, but in general all of the stars show typical kinematics of halo stars. The APOGEE DR17 spectroscopic results and Gaia eDR3 photometry are used to assess the stellar parameters and chemical properties of the stars. All of the stars belong to the red giant branch, and, in general, they follow the abundance pattern of typical halo stars. There are a few exceptions that would deserve further analysis through high-resolution spectroscopy. In particular, we identify a high-velocity Carbon-Enhanced Metal-Poor star, with a Galactocentric velocity of 482 km s^{-1}. We do not confirm any hypervelocity star in the sample, but this result is very sensitive to the adopted distances and less sensitive to the Galactic potential.

Unified Astronomy Thesaurus concepts: Milky Way dynamics (1051); Stellar kinematics (1608); Stellar abundances (1577)

1. Introduction

High-velocity stars in the Milky Way can be classified as bound or unbound stars to the Galaxy's gravitational potential. In the literature, such stars are also classified as runaway stars, hyper-runaway stars, hypervelocity stars (HVS), and high-velocity halo stars. The runaway stars are bound to the Galaxy and, as defined by Blaauw (1961), are OB-type stars with peculiar velocities faster than 40 km s^{-1} and with an origin in OB associations located in the Galactic disk. There are two main mechanisms for the production of runaway stars: supernova explosions in binary systems (Blaauw 1961), and dynamical interaction between massive stars in young clusters (Poveda et al. 1967).

Hyper-runaway or unbound runaway stars are stars that exceed the escape velocity of the Galaxy (Przybilla et al. 2008). Thermonuclear explosions of a white dwarf star orbiting another white dwarf (i.e., the "double-degenerate scenario") is one of the most likely channels to generate hyper-runaway stars (Shen et al. 2018). The first confirmed hyper-runaway star is HD 271791 with a Galactic rest-frame velocity of 630 km s^{-1}, and an apparent origin in the outer disk (Heber et al. 2008).

Unlike runaway/hyper-runaway stars with origin in the Galactic disk, HVS, as coined by Hills (1988), in principle originate in the center of the Galaxy, as a result of the interaction of binary stars with the supermassive black hole (Sgr A*) located in the center of the Milky Way (the "Hills mechanism"). Actually, these stars were theoretically predicted as evidence of the presence of a black hole in the center of the Galaxy (Hills 1988). The first hypervelocity star (HVS1) was observed by Brown et al. (2005) while searching for Blue Horizontal Branch (BHB) star candidates in the first data release of the Sloan Digital Sky Survey (SDSS), with the goal of spectroscopic follow-up observations with the 6.5 m Multiple Mirror Telescope (MMT). HVS1 is a B-type star with a Galactic rest-frame velocity of 673 km s^{-1} located in the halo at a current Galactocentric distance of $\sim$ 107 kpc (Brown et al. 2014).

Another interesting predicted population of high-velocity stars is that with an origin in globular clusters (Capuzzo-Dolcetta & Fragione 2015), and high-velocity stars with an origin in the Large Magellanic Cloud (LMC; Boubert & Evans 2016). Finally, high-velocity halo stars represent the extreme tail of the velocity distribution of this Galactic stellar population. In general, these could be an in situ population of stars (i.e., stars formed within the Milky Way; Di Matteo et al. 2019; Belokurov et al. 2020), or stars accreted during the numerous minor mergers that happened during the Galactic history formation (Pereira et al. 2012; Belokurov et al. 2018; Helmi et al. 2018; Koppelman et al. 2019; Myeong et al. 2019). Abadi et al. (2009) showed, through numerical simulation, that some halo stars acquire extreme kinematics as a result of near-radial infalls of parent dwarf galaxies that have subsequently been disrupted by tidal forces.

As we can see, the high-velocity stars are linked to extreme astrophysical phenomena in our Galaxy. Due to its kinematical characteristics and a large range of Galactocentric radii, this population of stars has been proposed as a sensitive dynamical tracer of the structure, shape, and dynamics of the Galaxy and its underlying, dark-matter-dominated gravitational potential (Gnedin et al. 2005; Yu & Madau 2007; Unwin et al. 2008; Piffl et al. 2014; Hattori et al. 2018a, 2018b). Nonetheless, until

recently, carrying out such analyses was challenged by limited access to precision measurements of all of the astrometric parameters (positions, proper motions, parallaxes) as well as radial velocities. As a consequence, the origin of the confirmed and candidate HVS was in debate, and some stars were found to be misidentified as HVS (Boubert et al. 2018).

This situation has been changing in recent years with the release of data from the Gaia astrometric mission (Gaia Collaboration et al. 2016) and ground-based spectroscopic surveys, such as the Apache Point Observatory Galactic Evolution Experiment (APOGEE; Majewski et al. 2017), GALactic Archaeology with HERMES (GALAH; Martell et al. 2017), and Large Sky Area Multi-Object Fiber Spectroscopic Telescope (LAMOST; Cui et al. 2012). On the one hand, Gaia provides high precision positions, trigonometric parallaxes, and proper motions, which together provide high-quality estimates (depending on a star's distance) of five out of six stellar phase space coordinates. On the other hand, the spectroscopic surveys, in addition to providing information on stellar atmospheric parameters and radial velocities, yield chemical abundance measurements that can be used to constrain the origin of the high-velocity stars via the concept of *chemical tagging* (Hawkins & Wyse 2018).

After the second Gaia data release (Gaia DR2; Collaboration et al. 2018), several new searches for high-velocity stars were published (Hattori et al. 2018a; Marchetti et al. 2019; Li et al. 2021), and some previous studies were revisited in light of the new astrometric data (Boubert et al. 2018; Brown et al. 2018; Irrgang et al. 2018; Kreuzer et al. 2020). Because, as these previous studies have shown, the synergy between Gaia and large-scale spectroscopic surveys allows for both discovery and a more complete and accurate kinematical and chemical characterization of high-velocity stars, we propose here to perform a similar investigation of the fastest stars in the APOGEE Data Release 17 (APOGEE DR17; Abdurro'uf et al. 2022). To do so, we exploit the Gaia early Data Release 3 (Gaia eDR3; Gaia Collaboration et al. 2021) as an essential part of verifying whether these stars belong to one of the high-velocity star populations previously mentioned. The data and quality control cuts used to select sources with reliable astrometric and spectroscopic measurements are described in Section 2. In Section 3 we present the process for determining positions and velocities in Galactocentric coordinates, and the selection of the high-velocity star candidates. In Section 4, we focus on the assessment of the orbital properties of this sample. The observed stellar properties are presented in Section 5. As a means to assess the potential origins of these high-velocity stars, we look at their detailed chemical abundances in Section 6. The main results are discussed in Section 7. Finally, our conclusions are summarized in Section 8.

2. Data

The chemical and astrometric data used in this work to search for and to characterize high-velocity stars come from the APOGEE DR17 and the Gaia eDR3, respectively. Since Gaia does not provide radial velocities for all stars, we use the radial velocities from APOGEE.

2.1. Gaia eDR3

Astrometric and photometric data used in this work come from observations of the Gaia satellite (Gaia Collaboration et al. 2016). This is an astrometric mission that aims to measure the positions and velocities of stars with precision on the order of tens of microarcseconds. Besides astrometric information, Gaia provides photometric data in the G, G_{BP}, and G_{RP} bands, and radial velocities for the brightest stars ($G_{\rm RVS} \lesssim 16.2$), measured with a radial velocity spectrograph with a resolution of ∼11,000 (Soubiran et al. 2018). More in-depth information about Gaia can be found in Brown (2021). In this work we use the Gaia eDR3 (Gaia Collaboration et al. 2021), which provides positions, parallaxes, and proper motions for ∼1.4 billion stars, of which ∼7 million have radial velocities already determined in Gaia DR2.

2.2. APOGEE DR17

All chemical information and radial velocities used to analyze the high-velocity stars come from the near-infrared (1.51–1.70 μm), multiobject, stellar spectroscopic survey APOGEE (Majewski et al. 2017), which is one of the main observational programs of the SDSS-III (Eisenstein et al. 2011) and SDSS-IV (Blanton et al. 2017) surveys. The APOGEE program corresponding to SDSS-IV is designated as APOGEE-2 and the APOGEE program corresponding to SDSS-III is designated simply as APOGEE. Unlike APOGEE, which conducted observations only from the Northern Hemisphere using the Sloan 2.5 m Telescope (Gunn et al. 2006), the installation of a second APOGEE spectrograph (Wilson et al. 2019) on the du Pont 2.5 m Telescope (Bowen & Vaughan 1973) enabled APOGEE-2 to conduct observations from both the Northern (APOGEE-2N) and the Southern (APOGEE-2S) Hemispheres.

Target selection for the two APOGEE surveys is described in Zasowski et al. (2013), Zasowski et al. (2017), Beaton et al. (2021), and Santana et al. (2021). Data products from spectra taken in both APOGEE surveys are included in SDSS DR17 (Abdurro'uf et al. 2022), after being automatically recalculated (Holtzman et al. 2015; Nidever et al. 2015) using the latest APOGEE data reduction pipeline, which uses an updated algorithm in DR17, `Doppler`,[5] for radial velocity determination; this algorithm has improved the derivation of radial velocities for fainter sources. The APOGEE Stellar Parameters and Chemical Abundances Pipeline (`ASPCAP`; García Pérez et al. 2016), which is rooted in the `FERRE`[6] code of Allende Prieto et al. (2006), provides atmospheric parameters ($T_{\rm eff}$, $\log g$, [Fe/H]) and chemical abundances measurements for up to 20 chemical species for 733 901 sources. `ASPCAP` estimates the stellar atmospheric parameters by comparing observed spectra against a library of MARCS stellar atmospheres (Mészáros et al. 2012; Jönsson et al. 2020), generated using an H-band line list from Smith et al. (2021), that updates the earlier APOGEE line list presented in Shetrone et al. (2015) to include the Ce and Nd line identifications from Cunha et al. (2017) and Hasselquist et al. (2016), respectively.

For the purpose of selecting stars with reliable radial velocity measurements, we perform a series of quality cuts in the APOGEE DR17 data. First, for any duplicated sources in the catalog, we select the entry with the higher signal-to-noise ratio (S/N) spectrum, $\texttt{S/N} > 10$, and we only select stars with an S/N-weighted velocity uncertainty $\texttt{VERR} < 1\ \mathrm{km\ s^{-1}}$. To reduce the impact of binary stars in our sample, we consider sources

[5] https://github.com/dnidever/Doppler
[6] https://github.com/callendeprieto/ferre

having a number of visits NVISITS > 1, and only consider stars with VSCATTER $< 1\,\mathrm{km\,s^{-1}}$. Also, the label ASPCAP-FLAG STAR_BAD (bit 23) was used to remove all the stars that are marked as STAR BAD. Finally, the STARFLAG bitmasks (bits 0, 3, 9, 4, 12, 13, 19, 22) are used to remove stars with issues associated with their radial velocity determination. These cuts reduce our sample to 370,301 sources.

3. High-velocity Stars Selection

Because our goal is to characterize stars with high velocity within the Milky Way, we consider stars with space velocity in Galactocentric coordinates (GC) greater than $450\,\mathrm{km\,s^{-1}}$, hereafter HiVel stars, close to the value considered in Li et al. (2021). To determine the positions and velocities in GC, it is necessary to have the full astrometric parameters (positions, proper motions, distances, and radial velocities). In our case, radial velocities are obtained from APOGEE DR17, and positions and proper motions from Gaia eDR3. At variance with the works of Hattori et al. (2018a), Marchetti et al. (2019), and Li et al. (2021), which use distances computed as the inverse of the parallax for sources with a positive parallax ($\varpi > 0$) and low fractional parallax error ($f = \sigma_\varpi/\varpi \leqslant 0.1$, 0.2), here we use the photogeometric distances estimated by Bailer-Jones et al. (2021). These distances were determined using a Bayesian probabilistic approach, in which the parallax is used to determine the geometric distances for nearby sources, and the magnitude and color given by the Gaia catalog are included to determine the photogeometric distances for distant sources. Alternative distances for APOGEE stars have been provided through two SDSS Value Added Catalogs: the StarHorse catalog, which uses photometric information from other catalogs to estimate the distance applying also a Bayesian approach (Anders et al. 2019, 2022), and the AstroNN catalog gives distances determined using a deep neural network (Leung & Bovy 2019). Since the distance has a direct effect on the GC velocity, we compare the distances obtained by the three catalogs and discuss their possible effect on our sample in Appendix A.

Since we do not consider the distance cutoff imposed by $f \leqslant 0.2$, our sample of stars will not only include nearby stars but also more distant stars. However, the GC velocities will depend on the priors assumed in the determination of the distances. Then, with the full astrometric parameters, the transformation from the International Celestial Reference System (ICRS) to GC coordinates is performed. The uncertainty propagation during the transformation is computed with 1000 Monte Carlo (MC) realizations using multivariate normal distributions $\mathcal{N}(\theta, \Sigma)$, where $\theta = (\alpha, \delta, \varpi, \mu_\alpha^*, \mu_\delta, v_r)$ are the observable parameters, and Σ is a 6×6 covariance matrix composed of the uncertainties and the correlation coefficients between the astrometric parameters provided by Gaia.[7] Then, each realization is transformed to GC coordinates, and we use the median, the 16th and 84th percentiles over the distributions in GC coordinates to get the position and velocity ($v_{\rm GC}$) for each star. This process was performed using the software Astropy (Astropy Collaboration et al. 2013, 2018) and the Pyia package (Price-Whelan 2018). The parameters used in the transformation were the parameters set by default in version 4.0 of the Astropy Galactocentric frame, where the distance from the Sun to the Galactic center is 8.122 kpc (Gravity Collaboration et al. 2018), the distance from the Sun to the Galactic midplane is 20.8 pc (Bennett & Bovy 2019), and the cartesian velocity of the Sun in the Galactocentric frame is $(12.9, 245.6, 7.78)\,\mathrm{km\,s^{-1}}$ (Drimmel & Poggio 2018).

After this process, we get a sample of 70 stars with velocities larger than $450\,\mathrm{km\,s^{-1}}$. However, this sample of stars was obtained without considering any cut on the Gaia data. In order to select a reliable sample of stars in Gaia, we only consider stars with a positive parallax ($\varpi > 0$). We also use the parameter ruwe < 1.4 to select sources with good astrometric solutions. Besides, using the catalog gedr3spur.main (Rybizki et al. 2022), hosted at the German Astrophysical Virtual Observatory (GAVO), we select stars with fidelity_v2 > 0.5, classified as good sources, and norm_dG < -3 to consider stars with good color measurement. Finally, as adopted by Marchetti et al. (2019), we select stars with relative error in GC velocity $\sigma_v/v_{\rm GC} < 30\%$. After all these considerations, we are left with a sample of 26 stars.

We further analyze the APOGEE spectra of these 26 stars, and we discard 3 stars that show problems in their spectra, not allowing us to obtain a reliable radial velocity. This left us with 23 stars, which constitute our final HiVel sample. Within this sample, nine stars have radial velocities determined both in Gaia eDR3 and APOGEE DR17, and we verified that they are in good agreement. Astrometric parameters and velocities for the HiVel stars are displayed in Tables 1 and 2.

3.1. Unbound Candidates

To identify if the HiVel stars are unbound candidates, we calculate for each star the probability of being unbound as the ratio of 1000 MC realizations resulting in a GC velocity $v_{\rm GC}$ higher than the escape speed from the Galaxy at the current position of the star

$$p_{ub} = n(v_{\rm GC} > v_{\rm esc})/1000,$$

as defined in Marchetti (2021). This is computed for the gravitational potential models of Irrgang Model I (Irrgang et al. 2013), McMillan (McMillan 2017), and MWPotential2014 (Bovy 2015), which are fully implemented in the galpy library (Bovy 2015). The red, gray, and green lines in Figure 1 represent the escape velocity curves calculated using the above-mentioned potentials. Filled markers correspond to stars with $f \leqslant 0.2$, which are the stars with more precise parallax. Open markers correspond to stars with $f > 0.2$. Orange markers are stars with GC velocities larger than $450\,\mathrm{km\,s^{-1}}$, and blue markers correspond to stars with velocities that exceed the escape velocity curve of the MWPotential2014 model but do not exceed the escape velocity of the other potentials. We refer to such three stars as the *unbound candidates*. Note, however, that the excess with respect to the MWPotential2014 escape velocity is within the 1σ uncertainties of the candidates' velocities.

4. Kinematics and Orbit Integrations

Using the positions and velocities in the left-handed GC reference frame, Figure 2 shows the HiVel stars' spatial distributions. The left panel shows the spatial distribution in the X–Y plane (the Galactic plane), and the right panel shows the spatial distribution in the X–Z plane. The horizontal dashed

[7] Correlation coefficients between radial velocity and the other parameters are assumed to be zero because they were measured with different instruments.

Table 1
Equatorial Coordinates, Parallaxes, and Distances for the HiVel Stars

APOGEE ID	α (deg $\pm$ mas)	δ (deg $\pm$ mas)	ϖ (mas)	$d_{\rm BJ}$ (kpc)
2M18333156-3439135	278.381 ± 0.013	−34.654 ± 0.012	0.077 ± 0.015	$7.134^{+1.024}_{-0.576}$
2M17183052+2300281	259.627 ± 0.006	23.008 ± 0.009	0.110 ± 0.011	$7.992^{+0.995}_{-0.728}$
2M00465509-0022516	11.730 ± 0.021	−0.381 ± 0.013	0.384 ± 0.024	$2.389^{+0.099}_{-0.089}$
2M17223795-2451372	260.658 ± 0.016	−24.860 ± 0.010	0.138 ± 0.018	$6.452^{+0.962}_{-0.646}$
2M18562350-2948361	284.098 ± 0.016	−29.810 ± 0.015	0.124 ± 0.021	$6.043^{+0.641}_{-0.532}$
2M17472865+6118530	266.869 ± 0.011	61.315 ± 0.011	0.172 ± 0.011	$5.348^{+0.241}_{-0.221}$
2M18070909-3716087	271.788 ± 0.015	−37.269 ± 0.014	0.127 ± 0.017	$6.550^{+0.510}_{-0.532}$
2M14473273-0018111	221.886 ± 0.029	−0.303 ± 0.028	0.062 ± 0.037	$8.766^{+1.162}_{-1.431}$
2M17145903-2457509	258.746 ± 0.018	−24.964 ± 0.011	0.079 ± 0.020	$6.963^{+0.823}_{-0.728}$
2M16323360-1200297	248.140 ± 0.024	−12.008 ± 0.013	0.090 ± 0.027	$6.968^{+0.963}_{-1.038}$
2M17122912-2411516	258.121 ± 0.054	−24.198 ± 0.033	0.035 ± 0.061	$8.469^{+0.964}_{-1.109}$
2M15191912+0202334	229.830 ± 0.014	2.043 ± 0.012	0.075 ± 0.016	$10.113^{+2.653}_{-1.815}$
2M17054467-2540270	256.436 ± 0.023	−25.674 ± 0.013	0.078 ± 0.026	$7.504^{+1.236}_{-0.836}$
2M16344515-1900280	248.688 ± 0.028	−19.008 ± 0.015	0.107 ± 0.035	$6.428^{+1.097}_{-1.069}$
2M22242563-0438021	336.107 ± 0.017	−4.634 ± 0.013	0.063 ± 0.018	$10.760^{+0.903}_{-0.879}$
2M18051096-3001402	271.296 ± 0.020	−30.028 ± 0.017	0.039 ± 0.022	$7.939^{+0.787}_{-0.809}$
2M18364421-3418367	279.184 ± 0.021	−34.310 ± 0.020	0.065 ± 0.028	$6.096^{+0.594}_{-0.453}$
2M17065425-2606471	256.726 ± 0.022	−26.113 ± 0.013	0.101 ± 0.024	$6.828^{+1.240}_{-0.793}$
2M17191361-2407018	259.807 ± 0.078	−24.117 ± 0.050	0.280 ± 0.094	$6.923^{+1.677}_{-2.083}$
2M17412026-3431349	265.334 ± 0.026	−34.526 ± 0.026	0.115 ± 0.041	$5.626^{+2.178}_{-1.321}$
2M14503361+4921331	222.640 ± 0.011	49.359 ± 0.014	0.103 ± 0.014	$7.457^{+0.675}_{-0.689}$
2M15180013+0209292	229.501 ± 0.014	2.158 ± 0.013	0.047 ± 0.015	$11.714^{+2.777}_{-1.449}$
2M19284379-0005176	292.182 ± 0.015	−0.088 ± 0.014	0.078 ± 0.019	$8.055^{+1.170}_{-0.943}$

Note. Parallaxes from Gaia eDR3. Distances from Bailer-Jones et al. (2021). The last three rows list the stars that exceed the escape velocity in the MWPotential2014 model (unbound candidates; Section 3.1).

lines in the X–Z plane marks the boundaries between the thick disk and the halo region. Some HiVel stars are in the disk region, while others fall in the halo region.

Aiming to identify how these stars behave kinematically, we use the Toomre diagram in Galactocentric cylindrical coordinates. This diagram is widely used in the literature and allows stars to be classified into Galactic populations using information based on the velocity components, without being necessary to assume a gravitational potential for the Galaxy. On the X-axis and Y-axis of Figure 3, we represent the azimuthal velocity component V_ϕ and the $\sqrt{V_R^2 + V_z^2}$ component, respectively. Stars with a kinetic behavior typical of the disk occupy the gray region in the plot. We conclude that all the HiVel stars behave kinetically as halo stars. We also see that some stars display retrograde ($V_\phi < 0$) motions, and others have prograde motions ($V_\phi > 0$).

4.1. Orbit Integration

Using the full information in the phase space (positions and velocities in GC), we perform back-in-time orbit integrations considering 1000 MC realizations for each star. The aim of this is twofold: (i) to calculate the orbital parameters, in order to confirm the kinematics of these stars, and (ii) to put constraints on the possible places of origin through the analysis of the stars' trajectories. For the orbit integration, we used the Irrgang Model I gravitational potential (Irrgang et al. 2013), implemented in `galpy`. This potential is an updated version of the classical Allen & Santillan (1991) model, and it is composed of a Plummer potential for the bulge, a Miyamoto–Nagai potential for the disk and a spherical potential for the Galactic halo. We choose this potential because recent results from Gaia DR2, using dynamical tracers like globular clusters and dwarf galaxies, is in agreement with this Model I parameters (Irrgang et al. 2018). Details about the model can be found in Appendix B.

Table 3 shows the orbital parameters obtained from a total integration time of 10 Ga. The left panel of Figure 4 shows the maximum distance above the Galactic plane ($Z_{\rm max}$) as a function of the orbital eccentricity (e). Since stars with similar orbits reside in specific regions of this plane, this kind of diagram was used by Boeche et al. (2013) to identify different populations of stars. We can see that the HiVel stars are highly eccentric ($e > 0.7$), and reach $Z_{\rm max} > 6$ kpc, similar to the halo stars in the Galaxy.

Aiming to put constraints on the spatial origin of the HiVel stars, we also compute the distance ($R_{\rm dc}$) to the Galactic center at the last intersection of the orbit with the disk plane. The left panel in Figure 5 shows $R_{\rm dc}$ as a function of the orbital energy; the stars 2M17054467-2540270 and 2M18051096-3001402 have $R_{\rm dc} \lesssim 1$ kpc, and within the uncertainties, they have a chance of being originated in the Galactic center. Such an origin for these sources needs to be analyzed in the context of chemical abundances that will be discussed below. The dashed vertical line in the figure divides the bound stars ($E < 0$) from the unbound stars ($E > 0$). All stars result to have bound orbits.

We perform an additional analysis including the integrations of the gravitational effect of the LMC. This analysis is justified because the LMC is the most massive dwarf galaxy satellite of

Table 2
Proper Motions, Radial Velocities, and Estimated Galactocentric Velocity for the HiVel Stars

APOGEE ID	$\mu_\alpha \cos\delta$ (mas yr^{-1})	μ_δ (mas yr^{-1})	$v_{\mathrm{rad_{APOGEE}}}$ (km s^{-1})	$v_{\mathrm{rad_{Gaia}}}$ (km s^{-1})	v_{GC} (km s^{-1})
2M18333156-3439135	-11.640 ± 0.017	-4.019 ± 0.014	-334.832 ± 0.779	...	$450.574^{+37.677}_{-17.739}$
2M17183052+2300281	-4.145 ± 0.008	-14.259 ± 0.010	18.794 ± 0.205	20.466 ± 0.645	$451.366^{+59.797}_{-44.668}$
2M00465509-0022516	-5.623 ± 0.031	17.908 ± 0.031	70.881 ± 0.083	70.188 ± 1.285	$463.276^{+8.803}_{-7.151}$
2M17223795-2451372	-1.433 ± 0.021	-5.171 ± 0.014	435.777 ± 0.096	435.660 ± 1.098	$463.408^{+2.867}_{-3.003}$
2M18562350-2948361	-0.471 ± 0.021	0.279 ± 0.018	356.485 ± 0.157	...	$464.402^{+0.380}_{-0.358}$
2M17472865+6118530	10.871 ± 0.017	-9.406 ± 0.015	-212.967 ± 0.110	-213.278 ± 0.839	$469.810^{+16.624}_{-14.870}$
2M18070909-3716087	11.487 ± 0.018	-4.047 ± 0.014	91.719 ± 0.204	90.634 ± 1.756	$482.896^{+23.944}_{-23.709}$
2M14473273-0018111	2.733 ± 0.039	-1.712 ± 0.039	342.836 ± 0.592	...	$453.063^{+7.665}_{-7.773}$
2M17145903-2457509	-3.426 ± 0.022	-6.802 ± 0.015	440.678 ± 0.622	441.401 ± 1.373	$454.279^{+1.370}_{-0.833}$
2M16323360-1200297	-8.011 ± 0.033	-2.397 ± 0.023	-463.083 ± 0.307	...	$459.954^{+7.701}_{-4.847}$
2M17122912-2411516	3.258 ± 0.070	-2.919 ± 0.049	-378.209 ± 0.718	...	$460.280^{+6.625}_{-6.593}$
2M15191912+0202334	4.066 ± 0.019	-9.831 ± 0.017	54.762 ± 0.122	55.099 ± 1.105	$470.407^{+108.852}_{-73.310}$
2M17054467-2540270	-15.615 ± 0.030	0.717 ± 0.019	55.665 ± 0.260	...	$478.116^{+88.233}_{-54.718}$
2M16344515-1900280	5.948 ± 0.038	-11.929 ± 0.024	295.646 ± 0.239	...	$481.088^{+42.192}_{-38.416}$
2M22242563-0438021	1.565 ± 0.021	-13.190 ± 0.015	-180.219 ± 0.076	...	$481.810^{+57.497}_{-56.742}$
2M18051096-3001402	1.347 ± 0.027	-9.845 ± 0.019	416.464 ± 0.131	...	$487.275^{+13.960}_{-12.253}$
2M18364421-3418367	-2.512 ± 0.027	-2.976 ± 0.023	458.399 ± 0.171	...	$492.254^{+2.015}_{-2.691}$
2M17065425-2606471	-3.017 ± 0.029	-14.325 ± 0.019	-437.308 ± 0.024	...	$507.591^{+50.363}_{-23.769}$
2M17191361-2407018	5.908 ± 0.102	-3.076 ± 0.072	357.739 ± 0.144	...	$508.340^{+28.941}_{-27.027}$
2M17412026-3431349	3.407 ± 0.034	-1.289 ± 0.024	456.415 ± 0.020	...	$526.611^{+10.700}_{-5.270}$
2M14503361+4921331	-15.377 ± 0.013	-13.192 ± 0.018	-120.268 ± 0.008	-123.121 ± 0.403	$512.687^{+59.956}_{-63.112}$
2M15180013+0209292	4.194 ± 0.019	-9.785 ± 0.017	54.910 ± 0.644	54.354 ± 0.804	$546.256^{+118.447}_{-61.675}$
2M19284379-0005176	-1.037 ± 0.020	-21.443 ± 0.017	-30.883 ± 0.234	...	$649.449^{+110.097}_{-90.470}$

Note. Proper motions from Gaia eDR3. Radial velocities from APOGEE DR17 and from Gaia eDR3 (when available). The last three rows correspond to the unbound candidates.

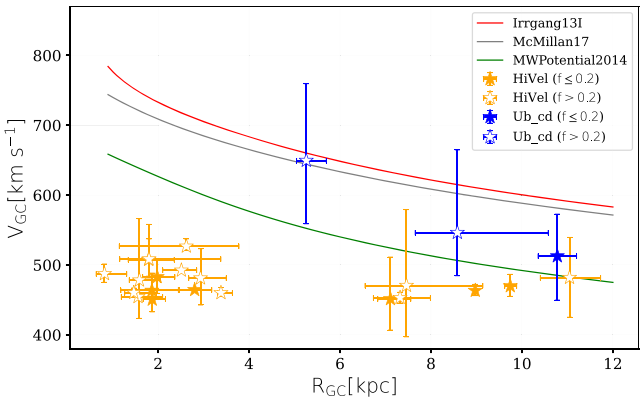

Figure 1. Galactocentric velocity as a function of the Galactocentric distance. Filled markers have $f \leqslant 0.2$ while hollow markers have $f > 0.2$. Orange markers represent stars with velocities > 450 km s^{-1}. Blue markers correspond to stars that exceed the escape velocity of the MWPotential2014 potential (unbound candidates). Red, gray, and green lines are the Galactic escape velocity curves from the Irrgang13I, McMillan17, and MWPotential2014 potentials, respectively.

the Milky Way, and it might have a relevant gravitational effect on the orbital evolution of the HiVel stars. We use the `MovingObjectPotential` function implemented in `galpy`. For the LMC gravitational potential, we consider a Plummer profile with a mass of $M_{\mathrm{LMC}} = 1.8 \times 10^{11}\, M_\odot$, taken from Shipp et al. (2021). The scale radius, $b = 17$ kpc, is calculated assuming an enclosed mass of $1.7 \times 10^{10}\, M_\odot$ within 8.7 kpc (van der Marel & Kallivayalil 2014).

In the right panels of Figures 4 and 5, we plot the Z_{max} and R_{dc} as functions of the eccentricity and orbital energy, respectively, including the effect of the LMC. The heights over the Galactic plane are slightly affected and the orbits of some stars become more eccentric, while the orbital energy slightly decreases. However, the kinematic behavior continues to be similar to that of the halo stars. For the orbit integrations taking into account the LMC, we calculate the minimum distance d_{LMC} between the star and the LMC during the integration. We find only one star (2M14503361+4921331) with a probability $p(d_{\mathrm{LMC}} < 5\ \mathrm{kpc}) = 0.18$ of passing within 5 kpc of the LMC, while all the other HiVel stars have $p(d_{\mathrm{LMC}} < 5\ \mathrm{kpc}) < 0.1$. It is worth noting that, in the above simulations, we do not take into account the dynamical friction force suffered by the LMC, which affects its orbit in time.

5. Stellar Parameters

Figure 6 shows the Hertzsprung–Russell (H-R) diagrams for the HiVel sample. The lines in green are theoretical evolutionary paths or isochrones for [Fe/H] = 1 and 10 Gyr age, obtained from the PAdova and TRieste Stellar Evolution Code (`PARSEC`; Bressan et al. 2012). On the left panel we plot the absolute G magnitudes against the BP–RP colors from Gaia eDR3. Because all the stars in the HiVel sample have a five-parameter astrometric solution, it is not necessary to apply the G-band photometry corrections (Riello et al. 2021). For our full sample, we carry out the dust extinction correction using the SFD2D dust map (Schlafly & Finkbeiner 2011), through the `dustmaps` package (Green 2018). In the right panel, we show the H-R diagram using the T_{eff} and

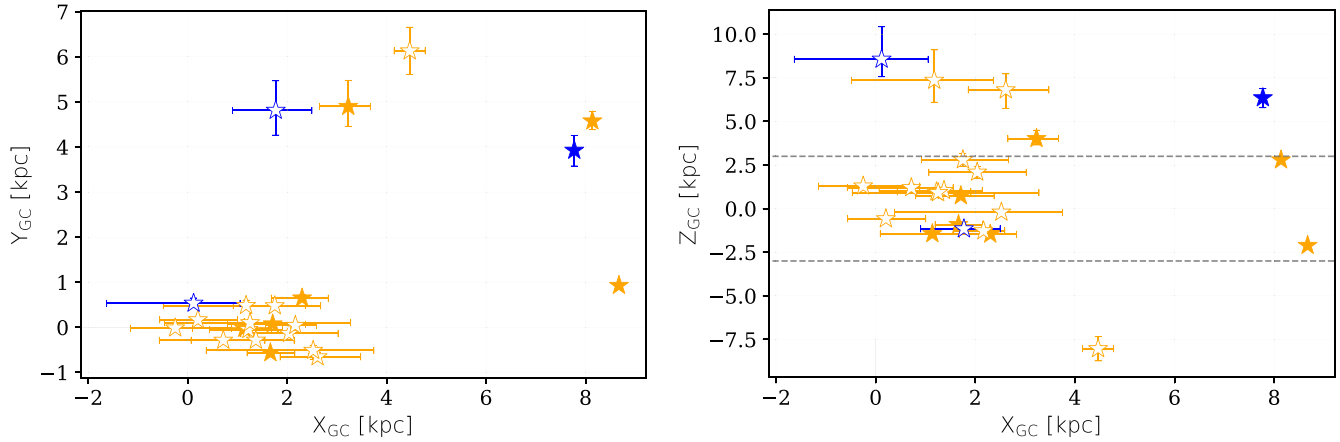

Figure 2. Spatial distribution of HiVel stars in the left-handed Galactocentric coordinates. Left, distribution in the X–Y plane. Right, distribution in the X–Z plane. Dashed horizontal lines indicate the transition between the thick disk and the halo. The Sun is located at $(X, Y, Z) = (8.12, 0.00, 0.02)$ kpc. Markers and colors are the same as in Figure 1.

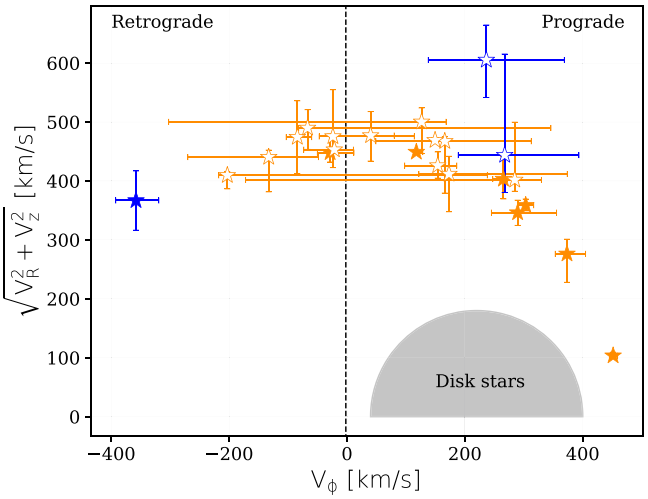

Figure 3. Toomre diagram of the HiVel sample. Markers and colors are the same as in Figure 1. The gray region represents stars with kinematic behavior typical of the disk. The dashed vertical line separates stars with retrograde and prograde motion.

$\log g$ from APOGEE DR17. All the HiVel stars are located in the Red Giant Branch (RGB).

Table 4 shows the stellar parameters for the HiVel sample, as determined from the APOGEE DR17 and Gaia eDR3 data. It is worth noting that the error of [α/Fe] reported in this table comes directly from the APOGEE DR17 file, and it represents the dispersion of the abundance value determined by the ASPCAP over the different visits to the same star. This strategy to estimate the uncertainty has been applied since DR16 (Jönsson et al. 2020) and differs from the empirical uncertainties derived in previous DRs by fitting the abundance scatter within stellar clusters (e.g., Holtzman et al. 2015; Jönsson et al. 2018). Nevertheless, for individual species, typical abundance uncertainties may range up to 0.1 dex, depending on the temperature and metallicity of the star and on the S/N of the spectrum (Jönsson et al. 2020). In most cases, the metallicities and α-elements abundances reported in Table 4 are typical of halo stars. A few peculiar cases will be discussed later in Section 7.

5.1. Masses and Radii

Using the stellar parameters $T_{\rm eff}$, $\log g$, and [Fe/H] from APOGEE DR17, the Gaia eDR3 parallaxes corrected by zero-point bias,[8] the G, BP, and RP magnitudes corrected by extinction, and the 2MASS magnitudes in the H, J, K bands, we infer the mass and radius of each star using the package `isochrones`. Among other features, this package uses the Mesa Isochrones & Stellar Tracks models (MIST; Paxton et al. 2011, 2013, 2015; Choi et al. 2016; Dotter 2016) to determine stellar properties based on arbitrary observables (Morton 2015). The results are reported in Table 5.

We note that there are five stars for which the isochrone-inferred masses are larger than $2\,M_\odot$, which would not be typical of halo stars. To check the reliability of these masses, we searched for an independent mass determination provided by the StarHorse2 catalog (Anders et al. 2022). The corresponding values are also reported in Table 5. We found that the StarHorse2 masses for three of these five stars is $\approx 1\,M_\odot$, consistent with halo stars. For the other two stars (2M15191912+0202334 and 2M15180013+0209292), there is no mass determination in the StarHorse2 catalog, but they have a mass estimate in the original StarHorse catalog (Anders et al. 2019) of $0.97^{+0.39}_{-0.16}\,M_\odot$ (27, $40\,R_\odot$) and $1.02^{+0.27}_{-0.18}\,M_\odot$ ($63.62\,R_\odot$), respectively. In view of this, we conclude that our isochrone-based mass determination for these five stars is most probably wrong.

On the other hand, for the remaining stars in the HiVel sample, our isochrone-based masses are in agreement with those of StarHorse2. The only exception is the star 2M17191361-2407018, for which StarHorse2 provides a mass of $2.24\,M_\odot$, against our value of $0.80\,M_\odot$. Nevertheless, the mass estimate for this star in the original StarHorse catalog is only $1.18^{+0.33}_{-0.20}\,M_\odot$ ($12.03\,R_\odot$), much closer to our value.

Assessing the sources of error that lead to estimating the wrong masses in some cases while not in others is beyond the scope of this work, although we believe that one possible source could be the bad quality values of $\log g$ provided by APOGEE. For example, if we apply the `isochrones` algorithm to the star 2M17412026-3431349, but we do not provide to the algorithm any information about the $\log g$ of the

[8] The correction is done using the `gaiadr3_zeropoint` Python package, hosted at https://gitlab.com/icc-ub/public/gaiadr3_zeropoint.

Table 3
Orbital Parameters Derived for the HiVel Stars in the Irrgang Model I Potential

APOGEE ID	$R_{\rm peri}$ (kpc)	$R_{\rm apo}$ (kpc)	e	$Z_{\rm max}$ (kpc)	E (km^2 s^{-2})
2M18333156-3439135	$1.40^{+0.28}_{-0.60}$	$12.61^{+4.87}_{-0.52}$	$0.80^{+0.12}_{-0.05}$	$12.57^{+4.80}_{-0.51}$	-161629^{+14663}_{-1602}
2M17183052+2300281	$4.74^{+0.88}_{-0.65}$	$57.48^{+67.38}_{-22.68}$	$0.85^{+0.07}_{-0.06}$	$38.45^{+44.24}_{-16.11}$	-92582^{+32264}_{-21546}
2M00465509-0022516	$8.75^{+0.06}_{-0.04}$	$81.66^{+9.65}_{-6.96}$	$0.81^{+0.02}_{-0.02}$	$18.34^{+4.32}_{-0.99}$	-77197^{+4520}_{-3610}
2M17223795-2451372	$0.63^{+0.12}_{-0.28}$	$14.19^{+4.30}_{-4.42}$	$0.92^{+0.02}_{-0.02}$	$6.20^{+1.28}_{-0.84}$	$-159900^{+13641}_{-21318}$
2M18562350-2948361	$2.08^{+0.23}_{-0.26}$	$21.74^{+2.40}_{-2.23}$	$0.83^{+0.00}_{-0.00}$	$9.43^{+0.37}_{-0.17}$	-136686^{+4940}_{-5149}
2M17472865+6118530	$8.48^{+0.17}_{-0.15}$	$99.59^{+24.02}_{-17.02}$	$0.84^{+0.03}_{-0.03}$	$67.41^{+15.30}_{-9.00}$	-69195^{+8769}_{-7615}
2M18070909-3716087	$1.82^{+0.43}_{-0.39}$	$17.38^{+1.85}_{-1.47}$	$0.81^{+0.05}_{-0.06}$	$14.33^{+2.51}_{-1.93}$	-146571^{+4415}_{-3655}
2M14473273-0018111	$7.03^{+0.59}_{-0.57}$	$63.56^{+13.87}_{-11.19}$	$0.80^{+0.02}_{-0.02}$	$63.05^{+7.45}_{-12.22}$	-87709^{+8176}_{-8117}
2M17145903-2457509	$0.18^{+0.11}_{-0.08}$	$11.85^{+2.93}_{-2.13}$	$0.97^{+0.01}_{-0.02}$	$9.42^{+3.35}_{-1.82}$	$-170460^{+12666}_{-11162}$
2M16323360-1200297	$1.73^{+0.55}_{-0.59}$	$27.77^{+2.76}_{-0.71}$	$0.88^{+0.04}_{-0.02}$	$26.71^{+2.56}_{-0.80}$	-125178^{+4366}_{-1191}
2M17122912-2411516	$0.41^{+0.45}_{-0.18}$	$11.46^{+4.19}_{-1.29}$	$0.93^{+0.03}_{-0.05}$	$9.48^{+1.58}_{-1.46}$	-168914^{+15243}_{-7569}
2M15191912+0202334	$4.90^{+4.24}_{-1.71}$	$80.47^{+668.97}_{-47.83}$	$0.89^{+0.09}_{-0.06}$	$80.10^{+195.29}_{-48.14}$	-78481^{+67471}_{-38755}
2M17054467-2540270	$0.93^{+0.73}_{-0.61}$	$13.00^{+26.04}_{-3.42}$	$0.92^{+0.05}_{-0.18}$	$12.75^{+25.04}_{-3.21}$	$-161549^{+51354}_{-12858}$
2M16344515-1900280	$0.48^{+0.40}_{-0.19}$	$28.87^{+14.18}_{-5.71}$	$0.97^{+0.01}_{-0.02}$	$25.73^{+17.08}_{-13.83}$	$-124089^{+18192}_{-10863}$
2M22242563-0438021	$9.86^{+0.92}_{-0.92}$	$143.20^{+232.11}_{-73.18}$	$0.87^{+0.07}_{-0.10}$	$140.93^{+217.03}_{-72.56}$	-54355^{+32468}_{-28938}
2M18051096-3001402	$0.21^{+0.16}_{-0.09}$	$8.35^{+4.07}_{-1.79}$	$0.95^{+0.02}_{-0.03}$	$6.02^{+3.19}_{-1.18}$	$-189533^{+21818}_{-13576}$
2M18364421-3418367	$0.66^{+0.17}_{-0.18}$	$25.97^{+3.64}_{-4.09}$	$0.95^{+0.01}_{-0.01}$	$13.08^{+2.10}_{-0.43}$	-129243^{+6150}_{-8428}
2M17065425-2606471	$0.46^{+0.23}_{-0.14}$	$21.23^{+7.15}_{-0.35}$	$0.96^{+0.01}_{-0.01}$	$19.14^{+4.94}_{-1.37}$	-138320^{+13488}_{-796}
2M17191361-2407018	$0.97^{+0.85}_{-0.56}$	$22.85^{+10.03}_{-5.60}$	$0.92^{+0.04}_{-0.03}$	$8.84^{+8.25}_{-4.98}$	$-135364^{+17308}_{-14145}$
2M17412026-3431349	$0.89^{+0.44}_{-0.51}$	$34.80^{+14.51}_{-17.44}$	$0.95^{+0.01}_{-0.03}$	$9.84^{+1.83}_{-2.41}$	$-115913^{+15721}_{-33836}$
2M14503361+4921331	$10.72^{+0.48}_{-0.43}$	$199.69^{+941.34}_{-110.96}$	$0.90^{+0.08}_{-0.11}$	$151.62^{+706.35}_{-80.66}$	-40949^{+34658}_{-32571}
2M15180013+0209292	$6.78^{+3.80}_{-1.60}$	$252.06^{+3238.42}_{-154.06}$	$0.95^{+0.05}_{-0.05}$	$202.81^{+1355.99}_{-105.19}$	-32646^{+82007}_{-37646}
2M19284379-0005176	$5.26^{+0.44}_{-2.38}$	$1302.64^{+2946.40}_{-1180.38}$	$0.99^{+0.01}_{-0.04}$	$803.96^{+1559.30}_{-694.01}$	-4113^{+82321}_{-57260}

Note. Perigalacticon and apogalacticon, orbital eccentricity, maximum height over the Galactic plane, and orbital energy. The last three rows correspond to the unbound candidates.

star, we obtain a mass estimate of 1.31 $M_\odot$, quite different from the 4.28 $M_\odot$ obtained when the algorithm is forced to use the $\log g$.

Concerning the radii, in general, the values that we estimate through the isochrones method are in agreement with the values derived from the $\log g$ and masses of StarHorse2. The largest discrepancies arise from the differences in $\log g$ and M between the catalogs. In any case, we conclude that our HiVel sample is composed of low-mass stars ($0.6 \lesssim M \lesssim 1\,M_\odot$), with big radii ($10 \lesssim R \lesssim 100\,R_\odot$), and low metallicities ($-2.2 \lesssim$ [Fe/H] $\lesssim -0.6$), consistent with halo stars belonging to the RGB.

6. Chemical Patterns

The analysis presented in Sections 4 and 5 has been done without taking into account the chemical information of the HiVel stars. In this section we use the chemical abundance ratios provided by APOGEE DR17 to try to shed light on the origin of these stars. This procedure is called *chemical tagging* (Freeman & Bland-Hawthorn 2002), and it was used, for example, by Hawkins & Wyse (2018) to analyze the origin of five HVS candidates in the Gaia DR2, reported by Marchetti et al. (2019). This concept was also used by Reggiani et al. (2022) to characterize fifteen HVS candidates selected from Hattori et al. (2018a) and Herzog-Arbeitman et al. (2018). In both cases, the chemical abundance ratios were obtained through high-resolution spectra.

For our HiVel sample, the analysis will be restricted to the chemical abundances of O, Mg, Al, Si, Mn, and Ni, which belong to the group of elements with very reliable measurements in APOGEE DR17. Except for the Mn abundances, available for only 17 stars, all the other elemental abundances are available for the entire HiVel sample. We discard the aluminum abundance for the star 2M19284379-0005176, which has the bitmask `AL_FE_FLAG` different from zero. As previously mentioned, the typical uncertainties in APOGEE abundances may range up to 0.1 dex, depending on temperature, metallicity, and S/N. Following the results of (Jönsson et al. 2020, their Figure 7), and taking into account the typical metallicities and temperatures of the HiVel stars, we may assume a mean uncertainty of ∼0.05 dex in the abundances of the six elements considered here.

6.1. Alpha Elements: Mg, Si, O

Alpha elements are a group of elements whose nucleus is composed of ^{4}He. According to chemical evolution models, the first α-elements were synthesized through the α process inside very massive stars, initially composed of He and H. After a period of time in which the star burns all its fuel, necessary to maintain the hydrostatic equilibrium, the core of the star collapses (type II supernovae), and then the elements of the outer layers of the star, composed mostly of α-elements and a lower fraction of iron-peak elements, are dispersed into the interstellar medium (ISM). Therefore, stars that formed from the material expelled by supernovae may be mostly enriched in α-elements. Subsequently, with a more favorable environment for the formation of low-mass stars, the production of metal-enriched stars increased, mainly through type Ia supernovae, so that the ratio between the abundance of α-elements and the

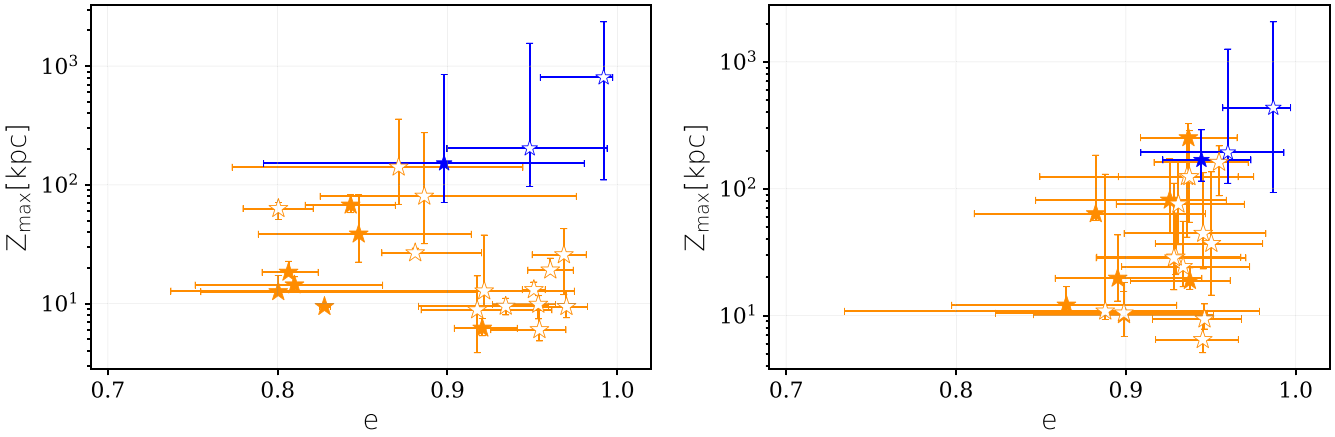

Figure 4. Maximum height over the Galactic plane (Z_{max}) reached during orbit integration as a function of orbital eccentricity (e). Markers and colors are the same as in Figure 1. Left, without the LMC. Right, including the LMC.

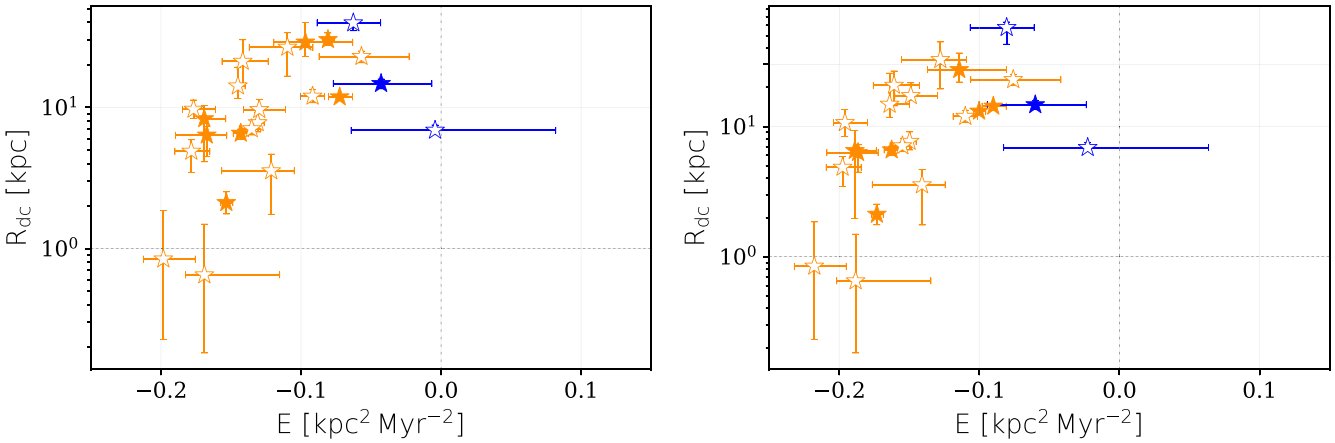

Figure 5. Distance from the Galactic center to the last intersection of the orbit with the Galactic plane (R_{dc}), as a function of the orbital energy. The vertical defines the limit between bounded (negative energy) and unbounded (positive energy) orbits. The horizontal line corresponds to a Galactocentric distance of 1 kpc, for reference. Markers and colors are the same as in Figure 1. Left: without the LMC. Right: including the LMC.

metallicity can be used to study the environment in which the stars formed.

The $[\alpha/\mathrm{Fe}] - [\mathrm{Fe/H}]$ for the stars in the Milky Way segregates the stars into three large groups, with not very well-defined boundaries between them, which correspond to the halo, thin disk, and thick disk, respectively. This is shown in the top-left panel of Figure 7, where the solid and dashed black lines have been adopted from Lane et al. (2022) as references. The gray regions in all panels of Figure 7 represent the density distribution obtained from the APOGEE DR17 data. Using the reference lines in the top-left panel to distinguish between the populations, we can conclude that most of the HiVel stars are metal-poor and are enriched in α-elements, like the halo stars. The unbound candidates (shown as blue stars) are clearly in the halo region, and some stars are in the boundary between the thin disk and the halo. The stars shown in red (2M18051096-3001402 and 2M17054467-2540270) are those that have a possible origin in the center of the Galaxy ($R_{dc} < 1$ kpc), and we can see that one of them is in the halo region while the other is in the boundary of the halo and the low-α thin disk.

On the other hand, we find a star (2M17183052+2300281) that seems to belong to the thick disk, and another star (2M22242563-0438021) with metallicity $[\mathrm{Fe/H}] = -1.79$ that appears to be very poor in α-elements. We will better discuss these two cases in Section 7.

6.2. Odd-Z Element: Al

Like the α-elements, the odd-Z elements are dispersed into the ISM mainly through type II supernovae. But unlike α-elements, these elements are strongly dependent on the metallicity of the parent star (Nomoto et al. 2013; Kobayashi et al. 2020a). The $[\mathrm{Al/Fe}] - [\mathrm{Fe/H}]$ distribution follows a characteristic pattern, that increases from low metallicities to $[\mathrm{Fe/H}] \sim -1$ and then decreases to about $[\mathrm{Fe/H}] \sim 0$ (Kobayashi et al. 2020a). The beginning of the decline is associated with the contribution of type Ia supernovae, which produce lower amounts of Al compared to Fe.

The middle-right panel of Figure 7 shows the $[\mathrm{Al/Fe}] - [\mathrm{Fe/H}]$ distribution for the HiVel sample. We verify that most HiVel stars have subsolar values of the $[\mathrm{Al/Fe}]$ ratios, which is also the case for the APOGEE halo stars in the figure, but one HiVel halo star appears slightly enriched in aluminum, and another one (2M15180013+0209292) is strongly enriched, with $[\mathrm{Al/Fe}] > +0.5$. This latter star is further discussed in Section 7.

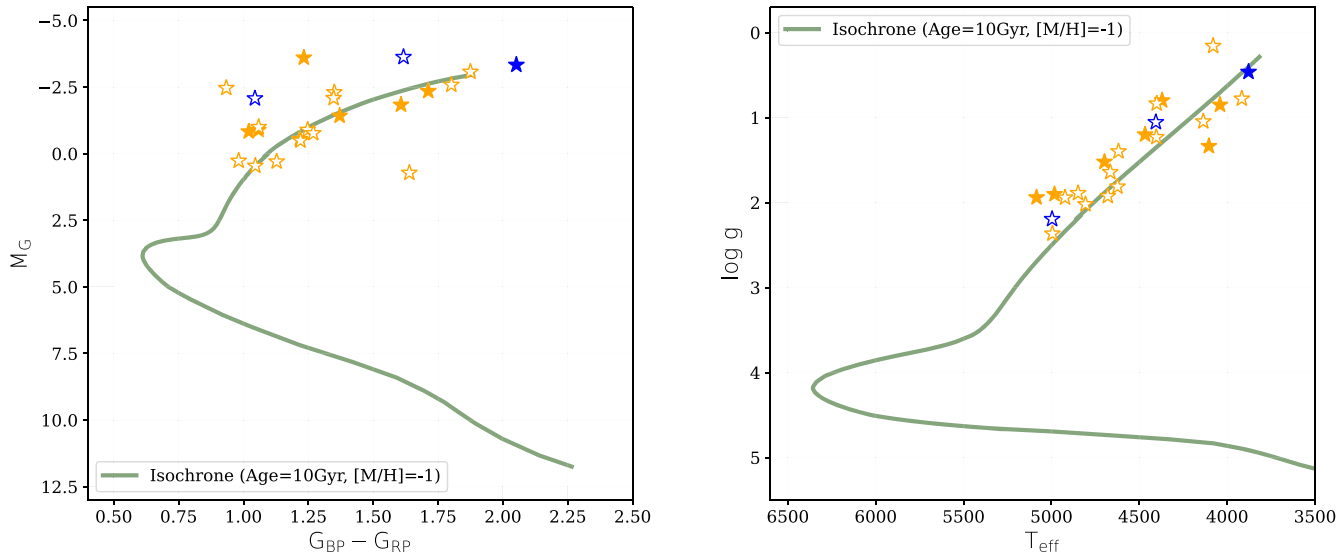

Figure 6. The H-R diagrams of the HiVel sample. The left panel shows the Gaia G absolute magnitude as a function of the Gaia BP–RP color. The right panel shows the surface gravity ($\log g$) as a function of the effective temperature ($T_{\rm eff}$). Markers and colors are the same as in Figure 1. Green lines indicate the stellar isochrones obtained from PARSEC.

Table 4
Observed Properties of the HiVel Stars

APOGEE ID	G (mag)	BP (mag)	RP (mag)	$T_{\rm eff}$ (K)	[Fe/H] (dex)	[α/Fe] (dex)
2M18333156-3439135	13.12	13.81	12.31	4467.51 ± 8.70	−1.21 ± 0.01	0.22 ± 0.01
2M17183052+2300281	12.79	13.59	11.92	4104.49 ± 5.91	−0.64 ± 0.01	0.32 ± 0.01
2M00465509-0022516	11.12	11.55	10.50	5084.93 ± 23.67	−1.70 ± 0.02	0.18 ± 0.03
2M17223795-2451372	12.63	13.86	11.54	4370.58 ± 9.60	−1.87 ± 0.01	0.23 ± 0.02
2M18562350-2948361	13.72	14.34	12.95	4698.49 ± 12.87	−1.22 ± 0.01	0.22 ± 0.01
2M17472865+6118530	12.86	13.32	12.21	4982.99 ± 13.41	−1.46 ± 0.01	0.26 ± 0.02
2M18070909-3716087	12.08	13.01	11.13	4041.14 ± 6.52	−1.19 ± 0.01	0.19 ± 0.01
2M14473273-0018111	15.29	15.75	14.65	4994.67 ± 29.81	−1.12 ± 0.02	0.27 ± 0.02
2M17145903-2457509	13.36	14.88	12.17	3917.18 ± 5.74	−1.01 ± 0.01	0.15 ± 0.01
2M16323360-1200297	14.89	15.75	13.96	4665.54 ± 16.34	−1.27 ± 0.02	0.21 ± 0.02
2M17122912-2411516	16.41	17.23	15.51	4922.99 ± 40.24	−1.52 ± 0.03	0.22 ± 0.03
2M15191912+0202334	12.82	13.46	12.06	4618.68 ± 9.45	−1.14 ± 0.01	0.16 ± 0.01
2M17054467-2540270	14.45	15.28	13.56	4401.37 ± 13.73	−0.85 ± 0.02	−0.07 ± 0.01
2M16344515-1900280	15.19	16.29	14.16	4848.71 ± 17.92	−1.22 ± 0.01	0.25 ± 0.02
2M22242563-0438021[a]	13.29	13.97	12.52	4136.07 ± 10.20[a]	−1.79 ± 0.02[a]	−0.38 ± 0.02[a]
2M18051096-3001402	13.10	14.65	11.89	4080.18 ± 8.10	−1.96 ± 0.01	0.10 ± 0.02
2M18364421-3418367	14.52	15.08	13.81	4806.53 ± 15.54	−1.22 ± 0.01	0.22 ± 0.02
2M17065425-2606471	14.44	15.30	13.53	4624.50 ± 16.68	−0.86 ± 0.02	0.11 ± 0.02
2M17191361-2407018	17.15	18.73	15.95	4679.61 ± 14.01	−0.80 ± 0.01	0.11 ± 0.01
2M17412026-3431349	14.40	15.75	13.25	4403.45 ± 8.74	−1.30 ± 0.01	0.24 ± 0.01
2M14503361+4921331	11.08	12.14	10.06	3878.89 ± 5.78	−1.15 ± 0.01	0.12 ± 0.01
2M15180013+0209292	11.82	12.61	10.95	4406.14 ± 8.15	−1.12 ± 0.01	0.11 ± 0.01
2M19284379-0005176	13.30	13.95	12.50	4996.48 ± 16.13	−2.18 ± 0.01	0.26 ± 0.03

Note. Absolute magnitudes from Gaia eDR3, effective temperature, metallicity, and α-elements abundance from APOGEE DR17. The last three rows correspond to the unbound candidates.
[a] The temperature, metallicity, and abundances provided by APOGEE DR17 for this star are most probably wrong and should be considered with caution. See Section 7.

6.3. Fe-peak Elements: Mn, Ni

The iron-peak elements ($21 \leqslant Z \leqslant 32$), in contrast to the α-elements and the odd-Z elements, are synthesized mostly via type Ia supernovae and, in less amount, via incomplete or complete Si-burning regions during core-collapse supernovae (Kobayashi et al. 2020b). The abundance distributions of iron-peak elements as a function of metallicity do not follow the same trends as the α and odd-Z elements. The bottom panels of Figure 7 show the [Mn/Fe] and [Ni/Fe] abundances as a function of metallicity. As expected by observations and Galactic chemical models, the Mn abundances decrease toward lower metallicities, and most HiVel stars follow this trend.

Table 5
Comparison of the $\log g$ Values from APOGEE DR17 and Derived Masses and Radii, with the Values Provided by the StarHorse2 Catalog

APOGEE ID	APOGEE DR17+isochrones			StarHorse2+Gaia eDR3		
	$\log g$	M ($M_\odot$)	R ($R_\odot$)	$\log g$	M ($M_\odot$)	R ($R_\odot$)
2M18333156-3439135	1.20 ± 0.04	$1.04^{+0.23}_{-0.25}$	$39.21^{+4.54}_{-4.50}$	$1.30^{+0.03}_{-0.01}$	$0.87^{+0.03}_{-0.08}$	34.59
2M17183052+2300281	1.34 ± 0.03	$0.93^{+0.07}_{-0.06}$	$40.29^{+2.04}_{-1.81}$	$1.16^{+0.01}_{-0.36}$	$0.95^{+0.03}_{-0.14}$	42.48
2M00465509-0022516	1.94 ± 0.06	$1.13^{+0.15}_{-0.17}$	$17.15^{+0.84}_{-0.70}$	$1.84^{+0.09}_{-0.10}$	$0.80^{+0.04}_{-0.03}$	17,82
2M17223795-2451372	0.80 ± 0.05	$3.64^{+0.49}_{-0.39}$	$90.46^{+8.89}_{-7.68}$	$0.88^{+0.69}_{-0.42}$	$1.05^{+3.40}_{-0.30}$	61.64
2M18562350-2948361	1.52 ± 0.04	$0.78^{+0.07}_{-0.02}$	$23.06^{+0.75}_{-0.57}$	$1.89^{+0.03}_{-0.01}$	$0.90^{+0.06}_{-0.07}$	17.84
2M17472865+6118530	1.90 ± 0.04	$1.15^{+0.20}_{-0.17}$	$18.52^{+1.54}_{-1.27}$	$1.79^{+0.14}_{-0.05}$	$0.77^{+0.07}_{-0.03}$	18.52
2M18070909-3716087	0.85 ± 0.04	$1.47^{+0.10}_{-0.59}$	$89.29^{+3.19}_{-13.42}$	$0.67^{+0.20}_{-0.16}$	$0.91^{+0.46}_{-0.31}$	73.08
2M14473273-0018111	2.37 ± 0.06	$1.15^{+0.08}_{-0.09}$	$10.71^{+0.43}_{-0.72}$	$2.52^{+0.02}_{-0.14}$	$0.83^{+0.04}_{-0.02}$	8.30
2M17145903-2457509	0.78 ± 0.03	$0.93^{+0.58}_{-0.09}$	$80.67^{+11.94}_{-3.65}$	$0.34^{+0.26}_{-0.04}$	$1.09^{+0.50}_{-0.34}$	116,95
2M16323360-1200297	1.64 ± 0.05	$0.80^{+0.10}_{-0.04}$	$23.14^{+1.02}_{-0.53}$	$1.83^{+0.38}_{-0.10}$	$0.86^{+0.01}_{-0.14}$	18.69
2M17122912-2411516	1.94 ± 0.09	$1.31^{+0.07}_{-0.08}$	$11.54^{+0.24}_{-0.55}$	$2.47^{+0.32}_{-0.07}$	$0.88^{+0.14}_{-0.04}$	9.05
2M15191912+0202334	1.40 ± 0.04	$2.22^{+0.08}_{-0.12}$	$46.12^{+0.96}_{-1.82}$	…	…	…
2M17054467-2540270	0.84 ± 0.05	$0.77^{+0.01}_{-0.00}$	$24.86^{+0.38}_{-0.38}$	$1.68^{+0.28}_{-0.19}$	$0.88^{+0.47}_{-0.08}$	22.47
2M16344515-1900280	1.89 ± 0.05	$2.78^{+0.02}_{-0.05}$	$28.16^{+0.32}_{-0.73}$	$1.74^{+0.43}_{-0.09}$	$0.81^{+0.12}_{-0.08}$	20.12
2M22242563-0438021	1.05 ± 0.05	$0.77^{+0.00}_{-0.00}$	$40.83^{+0.14}_{-0.15}$	$1.16^{+0.03}_{-0.11}$	$0.82^{+0.01}_{-0.09}$	39.46
2M18051096-3001402	0.16 ± 0.05	$0.87^{+0.20}_{-0.00}$	$95.93^{+10.28}_{-1.47}$	$0.17^{+0.07}_{-0.09}$	$0.59^{+0.05}_{-0.00}$	104.65
2M18364421-3418367	2.02 ± 0.05	$1.16^{+0.09}_{-0.12}$	$17.49^{+1.04}_{-1.30}$	$2.12^{+0.28}_{-0.38}$	$0.89^{+0.24}_{-0.09}$	13.61
2M17065425-2606471	1.81 ± 0.05	$0.88^{+0.36}_{-0.09}$	$20.85^{+3.39}_{-0.92}$	$1.77^{+0.01}_{-0.23}$	$0.90^{+0.03}_{-0.11}$	20.48
2M17191361-2407018	1.92 ± 0.04	$0.80^{+0.03}_{-0.02}$	$17.03^{+0.16}_{-0.20}$	$2.75^{+0.01}_{-0.09}$	$2.24^{+0.32}_{-0.61}$	10.46
2M17412026-3431349	1.23 ± 0.04	$4.28^{+0.18}_{-0.25}$	$53.71^{+3.83}_{-3.85}$	$0.77^{+0.13}_{-0.02}$	$0.75^{+0.15}_{-0.03}$	59.13
2M14503361+4921331	0.46 ± 0.03	$1.39^{+0.13}_{-0.15}$	$132.28^{+9.62}_{-7.35}$	$0.33^{+0.02}_{-0.00}$	$0.83^{+0.01}_{-0.00}$	103.24
2M15180013+0209292	1.05 ± 0.03	$3.17^{+0.17}_{-0.26}$	$91.37^{+4.01}_{-5.80}$	…	…	…
2M19284379-0005176	2.19 ± 0.06	$1.46^{+0.19}_{-0.15}$	$24.07^{+1.92}_{-2.95}$	$1.46^{+0.03}_{-0.02}$	$0.77^{+0.00}_{-0.03}$	27.07

Note. The StarHorse2 radius has been derived from the corresponding $\log g$ and M values (Anders et al. 2022). The two stars that do not have entries in the StarHorse2 catalog, have mass estimates in Anders et al. (2019); see text for details. The last three rows correspond to the unbound candidates.

However, there are two stars with an overabundance of Mn which would require further analysis.

7. Discussion

7.1. Dynamical and Chemical Constraints

The orbital parameters, the highly eccentric orbits, the fact of having stars with prograde motion and others with retrograde motion, and their location in the Toomre diagram, suggest that all HiVel stars have a kinematic behavior similar to halo stars. According to their location in the HR diagram, the estimated values for their masses, radii, and metallicities, the possibility of being OB runaway stars or hyper-runaway stars can be ruled out.

Taking into account that the potential energy, considering the Irrgang Model I potential, is less than zero for all the HiVel stars, and that it decreases even more when including the LMC, we may discard our unbound candidates as truly unbound stars. Moreover, these stars follow a chemical pattern similar to the halo stars, thus also ruling out an origin in the Galactic center or the Galaxy disk. The two bound stars with probable origin in the Galactic center ($R_{\rm dc} < 1$ kpc) may also be discarded because these stars follow a chemical pattern typical of halo stars.

From the orbital analysis, an origin in the LMC for the HiVel stars may also be ruled out. The only star that is likely to have a dynamical origin in the LMC (probability of 18%), is located, from the chemical point of view, in a region where the LMC chemistry overlaps with the chemical abundances of the largest dwarf galaxy that merged with the Milky Way, as shown in Figure 5 of Hasselquist et al. (2021). Therefore, it is difficult to identify an origin in the LMC when we only consider the O, Mg, Al, Si, and Mn abundances.

7.2. In Situ or Accreted Stars

Nissen & Schuster (2010) proposed that halo stars with metallicities between −1.8 and −0.4 can be divided into high-α and low-α populations. The first one would correspond to in situ stars (i.e., stars that formed in the Milky Way), while the second population would represent stars accreted during mergers over the Galaxy's evolution. Hayes et al. (2018) arrived at a similar conclusion, but analyzing the Mg abundances of the APOGEE DR13 halo stars, showing that they can be divided into high-Mg and low-Mg populations, the latter related to the accreted stars.

Figure 8 shows the distribution of α-elements abundances (left panel) and Mg abundances (right panel) against metallicities for the HiVel sample (color symbols) and for the APOGEE DR17 halo stars (gray dots). The latter have been selected according to the boundaries shown in Figure 7. The black dashed lines in both panels represent the limits between the in situ population (located in the top-right part of the plot) and the accreted population (located in the bottom-left part). For the α elements distribution, this limit has been defined from the Nissen & Schuster (2010) sample of halo stars. For the Mg abundances, the limit has been defined from the APOGEE DR13 stars considered in Hayes et al. (2018). It is worth noting

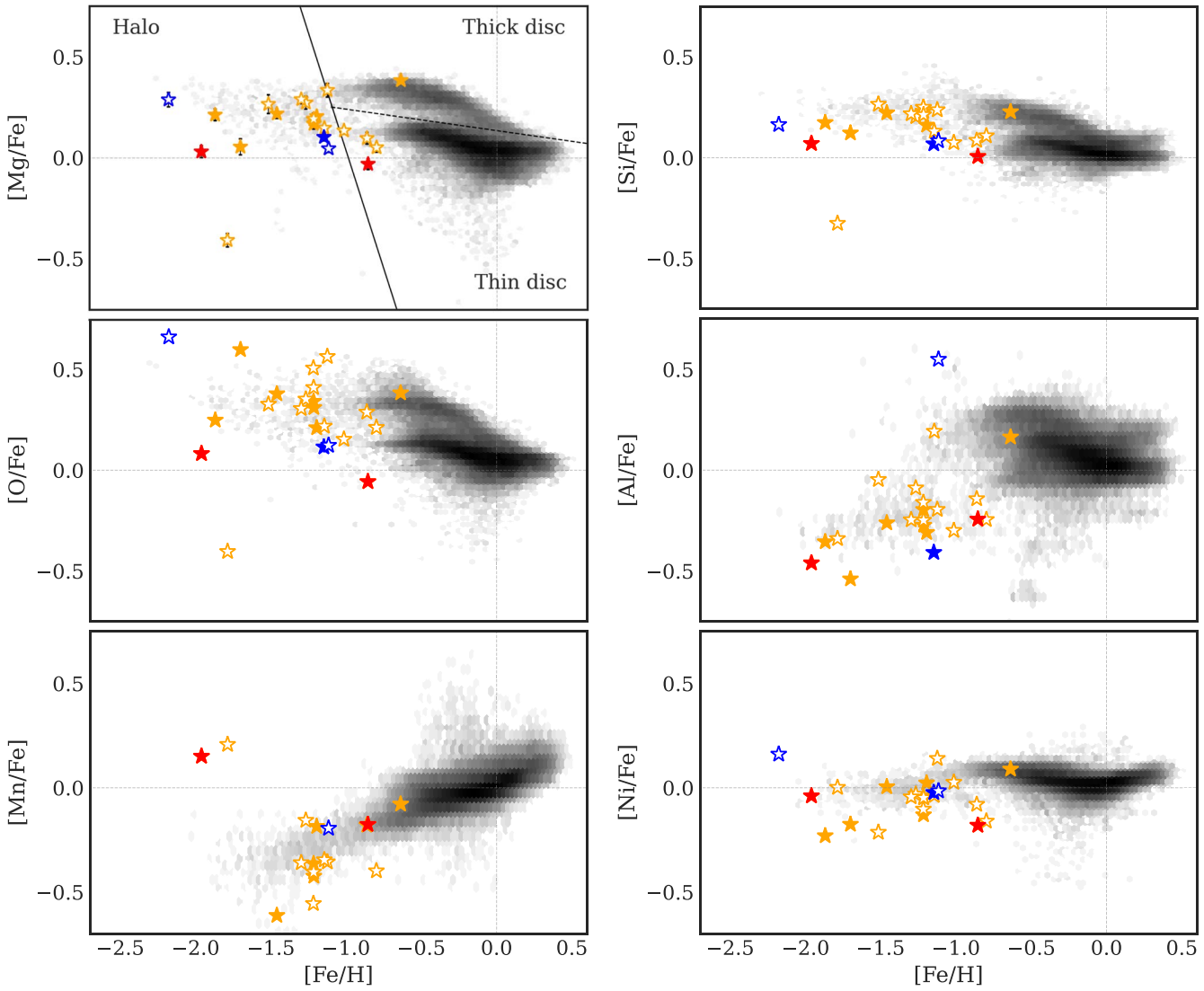

Figure 7. Abundances of individual elements as a function of metallicity. From top to bottom, left to right: α-elements (Mg, Si, O), odd-Z element (Al), and Fe-peak elements (Mn, Ni). Markers and colors are the same as in Figure 1, except for the red markers that correspond to the stars that might have an origin close to the Galactic center, from the kinematic point of view. The gray region represents the density distribution obtained from all the available APOGEE DR17 data. The solid and dashed lines in the top-left panel separate the halo stars from the disk stars, and the thin disk from the thick disk stars, respectively (Lane et al. 2022). The typical uncertainty in the abundances is ∼0.05 dex (Jönsson et al. 2020).

that, in both cases, most of the HiVel sample falls in the accreted population region (i.e., low-α or low-Mg).

We verify that there is a systematic difference between the Mg abundances of APOGEE DR13 and those in DR17. The latter are, on average, 0.06 dex higher than the former, with a dispersion of $\sigma = \pm 0.05$ dex. This implies that the black dashed line in the right panel of Figure 8 should be shifted up to the position of the gray dashed line, in order to establish the appropriate limit between low-Mg and high-Mg for DR17 data. In view of this, we may conclude that most of the HiVel stars in our sample belong to a low-α halo population of probably accreted stars. According to Hawkins et al. (2015) and Belokurov & Kravtsov (2022), this result would also be supported by the abundance of aluminum with subsolar values observed in Figure 7.

In Appendix C, we also present additional dynamical arguments supporting the hypothesis of an accreted origin of most HiVel stars.

7.3. Peculiar Cases

From the analysis of the chemical abundances, we find three stars that do not follow the expected chemical pattern of halo stars. We discuss these three peculiar stars in the following.

2M22242563-0438021 (HE 2221-0453)—This star has been classified in the literature as a Carbon-Enhanced Metal-Poor star (CEMP), based on high-resolution optical spectroscopic analysis (Aoki et al. 2007; Yoon et al. 2016). In particular, Aoki et al. (2007) provide radial velocity measurement for this star that is in good agreement with APOGEE's value. However, these authors also provide very different results for the stellar parameters, metallicity, and all the measured abundances compared to the values estimated by APOGEE DR17. The fact of being a CEMP star may explain the big differences that are evident in Table 6. With a true carbon abundance ratio [C/Fe] = 1.83, for example, this star falls outside the grid of models that are used by ASPCAP. Therefore, although ASPCAP is able to find a good fit to the APOGEE

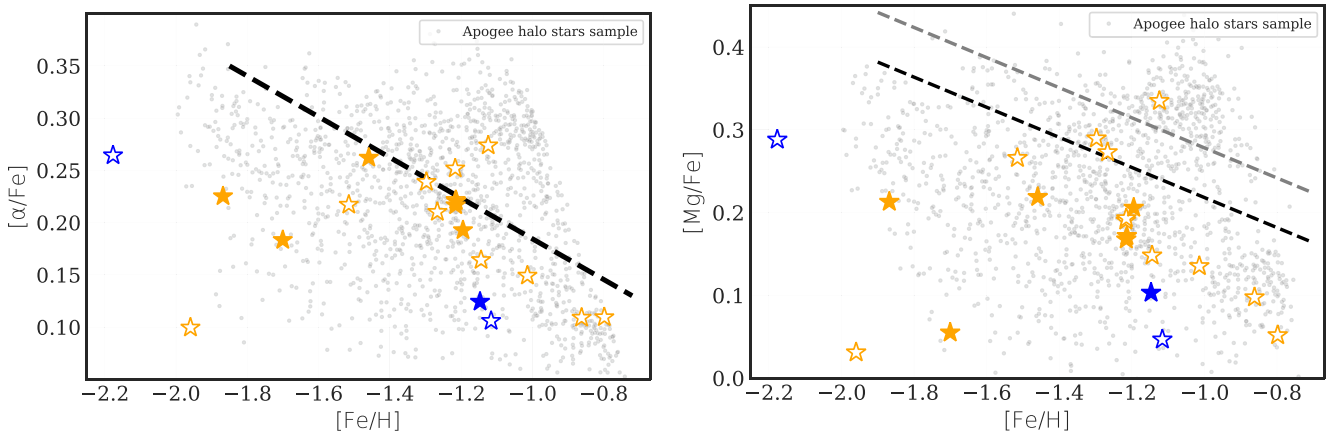

Figure 8. Halo stars in the [α/Fe] vs. [Fe/H] space (left), and the [Mg/Fe] vs. [Fe/H] space (right). Markers and colors for the HiVel sample are the same as in Figure 1. Gray dots are all the halo stars from APOGEE DR17. The black dashed lines separate the high-α or high-Mg (in situ) population from the low-α or low-Mg (accreted) population, as defined by Nissen & Schuster (2010; left) and Hayes et al. (2018; right). The gray dashed line in the right panel is the corrected limit accounting for the systematic differences in Mg abundances between APOGEE DR13 and DR17. Typical uncertainties in [Mg/Fe] are below 0.05 dex (Jönsson et al. 2020).

Table 6
Comparison of Stellar Parameters, Chemical Abundances [X/Fe], and Radial Velocities of the Star 2M22242563-0438021 (HE 2221-0453)

	Aoki et al. (2007)	APOGEE DR17
$T_{\rm eff}$ (K)	4400	4136
log g	0.4	1.04
[Fe/H]	−2.2	−1.79
Mg	0.8	−0.4
Ca	0.82	−0.56
C	1.83	0.53
N	0.84	0.08
Ti	0.54	−0.68
$v_{\rm rad}$ (km s^{-1})	−189.9	−180.2

Note. All abundances are in dex.

spectrum of this star, that fit corresponds to a local minimum within the model grid and does not represent the actual solution. We have verified by manual synthesis that both Aoki et al.'s solution and ASPCAP solution provide good fits to the APOGEE observed spectrum, with similar χ^2 residuals. But the ASPCAP solution is abnormally poor in α-elements, as well as abnormally enriched in Mn, being totally outside the expected trend for halo stars. Thus, there is no doubt that Aoki et al.'s solution is the correct one. On the other hand, the radial velocity of this star is well determined by APOGEE, so its classification in the HiVel sample is still valid, turning this star a rare, if not the first, an example of a high-velocity CEMP star. Aoki et al. (2007) provide a barium abundance of [Ba/Fe] = 1.75, leading to classify this star as a CEMP-s, which would imply to be a binary star. However, since europium abundance has not been determined, it cannot be confirmed as a truly CEMP-s. A discussion on the possible binary character of this star would depend on precise measurements of radial velocity variations, that do not exist in the literature.

2M17183052+2300281—This star is the most metal-rich in our sample, and belongs to the thick disk region (high-α sequence) in the [Mg/Fe] – [Fe/H] space. It follows well the abundance pattern of the thick disk stars. Mackereth et al. (2019), combining data from APOGEE DR14, Gaia DR2, and orbital eccentricity, show a large sample of highly eccentric stars located in the thick disk region. Belokurov et al. (2020) argued that these stars belong to a special population of stars dubbed the *Splash population*, formed in the Galaxy (i.e., in situ stars). An important parameter to probe if this star belongs to this population would be its age, since it is believed that such stars are younger than the stars belonging to the satellite galaxies that merged with our Galaxy. However, age determinations for individual stars belonging to the RGB are quite uncertain and difficult to obtain.

2M15180013+0209292—This star is one of the unbound candidates. It is highly enriched in aluminum and is also enriched in nitrogen, [N/Fe] $\sim$ 1. These features fit well to the population of stars reported by Fernández-Trincado et al. (2020), who based on the kinematic and chemical analysis of 29 stars, proposed that such stars were probably accreted from globular clusters by the Galaxy during the mergers experienced by the Milky Way in the past.

8. Conclusions

In this work, we have analyzed a sample of 23 high-velocity stars that we identified in the APOGEE DR17 catalog. The Galactocentric velocities of these stars were derived by combining the Gaia eDR3 proper motions, the Bailer-Jones et al. (2021) distances, and the APOGEE DR17 radial velocities. Our conclusions can be summarized as follows:

1. We found three stars that are unbounded to the MWPotential2014 galactic potential, but they are bounded to the Irrgang Model I potential. Twenty other stars display velocities greater than 450 km s^{-1}, but they are all bounded to the Galaxy. Including the gravitational effect from the LMC tends to make the stars even more bounded to the Milky Way.
2. From the kinematic point of view, all the stars are typical halo stars. Two stars in the sample passed close to the Galactic center (<0.9 kpc) in the past, but not close enough to allow the invoking of the Hills mechanism as the source of their high velocity.
3. Stellar parameters provided by APOGEE spectra and Gaia photometry indicate that the stars belong to the RGB ($0.6 \lesssim M \lesssim 1\,M_{\odot}$; $10 \lesssim R \lesssim 100\,R_{\odot}$). Stars are metal-poor ($-2.2 \lesssim$ [Fe/H] $\lesssim -0.6$) and show abundances that,

in most cases, are compatible with low-α halo stars (accreted stars).
4. One star shows unusually low abundances of all the α-elements, while is enriched in Mn. This star resulted to be a CEMP star, previously identified in the literature, whose abundances are not properly determined by the APOGEE automatic reduction pipeline. It is a peculiar example of a high-velocity ($v_{GC} = 482\,km\,s^{-1}$) CEMP star.
5. The most metal-rich star in the sample ([Fe/H] $\simeq -0.6$) appears to belong to the thick disk.
6. One of the fastest stars in the sample ($v_{GC} = 546\,km\,s^{-1}$) is unusually enriched in Al, Ni, and O. This star would deserve further analysis through high-resolution spectroscopy.
7. We did not identify any confirmed hypervelocity star in the APOGEE DR17, but we found some stars that are borderline. Classification of such stars as HVS is sensitive to the adopted distances.
8. Taking into account the uncertainties in the estimated Galactocentric velocities, the classification of HVS stars seems to be not too sensitive to the assumed potential for the Galaxy.
9. The fact that most stars in the sample follow an abundance pattern typical of accreted stars seems compatible with the idea that their high velocities originated in strong dynamical interactions during mergers of dwarf galaxies with the Milky Way.

This work has been partially financed by the Coordenação de Aperfeiçoamento de Pessoal de Nível Superior—Brasil (CAPES), Finance Code 001. FR and CBP are grateful for the financial support from the Brazilian National Council of Research—CNPq.

Funding for the Sloan Digital Sky Survey IV has been provided by the Alfred P. Sloan Foundation, the U.S. Department of Energy Office of Science, and the Participating Institutions. SDSS acknowledges support and resources from the Center for High-Performance Computing at the University of Utah. The SDSS website is www.sdss.org.

SDSS is managed by the Astrophysical Research Consortium for the Participating Institutions of the SDSS Collaboration including the Brazilian Participation Group, the Carnegie Institution for Science, Carnegie Mellon University, Center for Astrophysics | Harvard & Smithsonian (CfA), the Chilean Participation Group, the French Participation Group, Instituto de Astrofísica de Canarias, The Johns Hopkins University, Kavli Institute for the Physics and Mathematics of the Universe (IPMU)/University of Tokyo, the Korean Participation Group, Lawrence Berkeley National Laboratory, Leibniz Institut für Astrophysik Potsdam (AIP), Max-Planck-Institut für Astronomie (MPIA Heidelberg), Max-Planck-Institut für Astrophysik (MPA Garching), Max-Planck-Institut für Extraterrestrische Physik (MPE), National Astronomical Observatories of China, New Mexico State University, New York University, University of Notre Dame, Observatório Nacional/MCTI, The Ohio State University, Pennsylvania State University, Shanghai Astronomical Observatory, United Kingdom Participation Group, Universidad Nacional Autónoma de México, University of Arizona, University of Colorado Boulder, University of Oxford, University of Portsmouth, University of Utah, University of Virginia, University of Washington, University of Wisconsin, Vanderbilt University, and Yale University.

Appendix A
Distances

All our analysis of the HiVel stars is based on the photogeometric distances estimated by Bailer-Jones et al. (2021). Since the velocity of a star is most sensitive to its distance, it is important to compare the adopted distances to other estimates available in the literature. We consider here the StarHorse2 catalog (Anders et al. 2022) and the AstroNN catalog (Leung & Bovy 2019), as well as the distances obtained as the inverse of the Gaia parallax.

The Bailer-Jones catalog uses information on parallaxes and colors from the Gaia eDR3 to estimate the distances. For nearby sources, the distance is computed directly from the parallax, but for distant sources, the authors used a Bayesian inference method that provides the posterior distribution of distances depending on the given priors. The priors are taken from a synthetic mock catalog of the eDR3 (Rybizki et al. 2020), which gives the positions, distances, magnitudes, colors, and extinctions of 1.5 billion individual stars. This mock catalog covers well the population of RGB halo stars, and it is expected to provide good distance estimates of our HiVel stars.

The StarHorse2 catalog also uses a Bayesian inference to estimate distances, but is based on a different set of parameters and priors (Queiroz et al. 2018). The catalog combines information on stellar parameters (temperature, surface gravity, metallicity, etc.) from other catalogs, including APOGEE (Queiroz et al. 2020). In particular, it assumes Gaussian priors for age and metallicity, which are broad enough to accommodate most or all of the recent distributions found in the literature. Metallicity priors, for example, follow a distribution with -0.6 ± 0.5 for the thick disk, and -1.6 ± 0.5 for the halo, which encompasses well the metallicity range of our HiVel stars.

Finally, the AstroNN catalog combines two deep neural networks to estimate the distances. One network is trained using Gaia magnitudes and colors, and the other is trained using normalized continuum spectra obtained from APOGEE and the pseudoluminosity obtained from the 2MASS K_S band. This training set is also expected to encompass well the stars in our HiVel sample.

The comparisons between the catalogs are shown in Figure 9. It is worth noting that some HiVel stars do not have distance estimates in either StarHorse2 or AstroNN.

Gaia parallaxes provide, in general, much larger distances than Bailer-Jones, but this is not surprising since the latter is precisely an unbiased set of the former. If we use the Gaia parallaxes directly, many HiVel stars will be misidentified as HVS.

The situation is more consistent when compared to StarHorse2 distances that, in general, show a good agreement. The only exception is 2M17412026-3431349, which has a StarHorse2 distance of about twice its Bailer-Jones distance, although with such StarHorse2 distance it still remains bound to the Galaxy. On the other hand, star 2M22242563-0438021 shows a difference in distance of only 0.1 kpc between the two catalogs, but this is enough to turn it into an unbound candidate when assuming the StarHorse2 distance. We recall that this is the peculiar CEMP star in our sample.

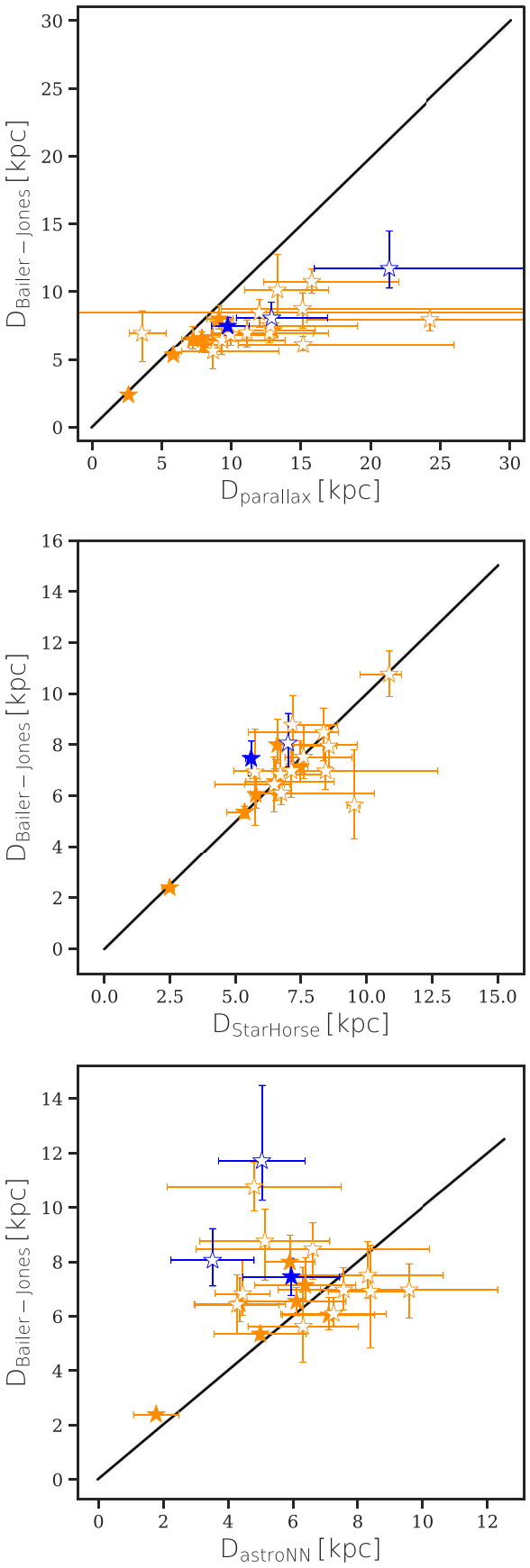

Figure 9. Comparison between the photogeometric distances of Bailer-Jones et al. (2021) used in this work (vertical axis) and other distance estimates for the HiVel stars: Gaia parallaxes (top panel), StarHorse2 (middle panel), and AstroNN (bottom panel). Markers and colors are the same as in Figure 1.

The comparison to AstroNN distances shows bigger dispersion. In general, AstroNN provides much smaller distances for the HiVel stars than Bailer-Jones. The three candidates that we found to be unbounded to the MWPotential2014 become bounded according to the AstroNN distances, and they will not be classified as HiVel stars either. Actually, many stars in our HiVel sample show Galactocentric velocities smaller than 450 km s^{-1} when assuming the AstroNN distances.

Appendix B
Model I Gravitational Potential

The Model I gravitational potential described in Irrgang et al. (2013) is a revised version of the Allen & Santillan (1991) potential. The bulge is modeled as a Plummer potential:

$$\Phi_b(R, z) = -\frac{GM_b}{\sqrt{R^2 + b_b^2 + z^2}}, \tag{B1}$$

where (R, z) are the components of the cylindrical coordinate system. The disk is axisymmetric and modeled by a Miyamoto–Nagai potential (Miyamoto & Nagai 1975):

$$\Phi_d(R, z) = -\frac{GM_d}{\sqrt{R^2 + (a_d + \sqrt{b_d^2 + z^2})^2}}. \tag{B2}$$

Finally, the galactic halo is modeled by a spherical potential given by:

$$\Phi_h(R, z) = \begin{cases} \frac{GM_h}{a_h}\left[\frac{1}{\gamma - 1}\ln\left(\frac{1 + (r/a_h)^{\gamma-1}}{1 + \beta^{\gamma-1}}\right) \right. \\ \qquad \left. - \frac{\beta^{\gamma-1}}{1 + \beta^{\gamma-1}}\right], & \text{if } r < \Lambda, \\ -\frac{GM_h}{r}\frac{\beta^{\gamma}}{1 + \beta^{\gamma-1}}, & \text{if } r \geqslant \Lambda, \end{cases} \tag{B3}$$

where $\beta = \Lambda/a_h$, M_b, M_d, and M_h are the masses of the components in Galactic mass ($M_{\rm Gal} = 2.325 \times 10^7\, M_\odot$), b_b, a_d, b_d, and a_h are the scale lengths of the components, and $r = \sqrt{R^2 + z^2}$. The values of these parameters are given in Table 7.

Table 7
Irrgang Model I Parameters

M_b ($M_{\rm Gal}$)	409 ± 63
M_d ($M_{\rm Gal}$)	2856^{+376}_{-202}
M_h ($M_{\rm Gal}$)	1018^{+27933}_{-603}
b_b (kpc)	0.23 ± 0.03
a_d (kpc)	$4.22^{+0.53}_{-0.99}$
b_d (kpc)	$0.292^{-0.025}_{+0.020}$
a_h (kpc)	$2.562^{+25.963}_{-1.419}$
Λ (kpc)	200^{+0}_{-83}
γ	2

Appendix C
Action Diamond Space

Figure 10 shows the place occupied by the HiVel stars in the action diamond space. The actions are calculated using `galpy` considering the Stackel approximation (Binney 2012) and the Irrgang Model I potential. Most of the stars lie in the region of highly radial orbits, as expected. The green box, adopted from

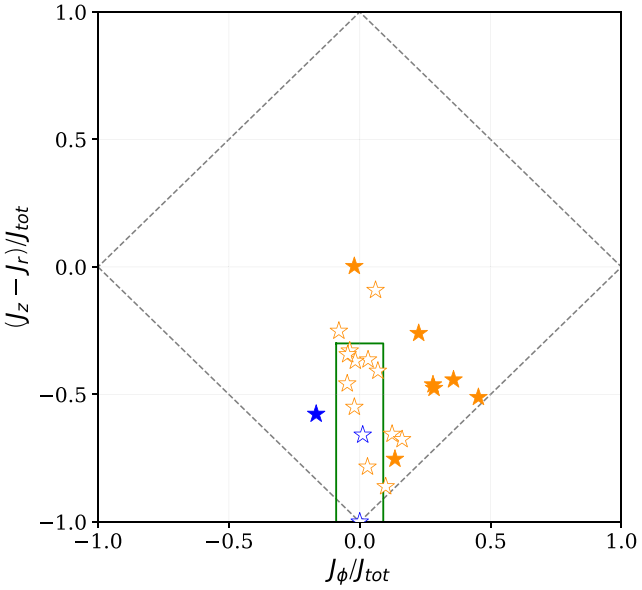

Figure 10. Distribution of the HiVel sample in the action diamond space. Markers and colors are the same as in Figure 1. The green box represents the locations of the Gaia-Sausage remnant.

Monty et al. (2020), is the region that would be occupied by stars belonging to the Gaia-Sausage-Enceladus dwarf galaxy, that merged with the Milky Way. Several HiVel stars fall in this region, reinforcing their possible origin as accreted stars.

ORCID iDs

F. Quispe-Huaynasi https://orcid.org/0000-0001-8741-8642
F. Roig https://orcid.org/0000-0001-7059-5116
D. J. McDonald https://orcid.org/0000-0002-9448-6261
V. Loaiza-Tacuri https://orcid.org/0000-0003-0506-8269
S. R. Majewski https://orcid.org/0000-0003-2025-3147
F. C. Wanderley https://orcid.org/0000-0003-0697-2209
K. Cunha https://orcid.org/0000-0001-6476-0576
S. Hasselquist https://orcid.org/0000-0001-5388-0994
S. Daflon https://orcid.org/0000-0001-9205-2307

References

Abadi, M. G., Navarro, J. F., & Steinmetz, M. 2009, ApJL, 691, L63
Abdurro'uf, Accetta, K., Aerts, C., et al. 2022, ApJS, 259, 35
Allen, C., & Santillan, A. 1991, rmxaa, 22, 255
Allende Prieto, C., Beers, T. C., Wilhelm, R., et al. 2006, ApJ, 636, 804
Anders, F., Khalatyan, A., Chiappini, C., et al. 2019, A&A, 628, A94
Anders, F., Khalatyan, A., Queiroz, A. B. A., et al. 2022, A&A, 658, A91
Aoki, W., Beers, T. C., Christlieb, N., et al. 2007, ApJ, 655, 492
Astropy Collaboration, Robitaille, T. P., Tollerud, E. J., et al. 2013, A&A, 558, A33
Astropy Collaboration, Price-Whelan, A. M., Sipőcz, B. M., et al. 2018, AJ, 156, 123
Bailer-Jones, C. A. L., Rybizki, J., Fouesneau, M., Demleitner, M., & Andrae, R. 2021, AJ, 161, 147
Beaton, R. L., Oelkers, R. J., Hayes, C. R., et al. 2021, AJ, 162, 302
Belokurov, V., Erkal, D., Evans, N. W., Koposov, S. E., & Deason, A. J. 2018, MNRAS, 478, 611
Belokurov, V., & Kravtsov, A. 2022, MNRAS, 514, 689
Belokurov, V., Sanders, J. L., Fattahi, A., et al. 2020, MNRAS, 494, 3880
Bennett, M., & Bovy, J. 2019, MNRAS, 482, 1417
Binney, J. 2012, MNRAS, 426, 1324
Blaauw, A. 1961, Bull. Astron. Inst.Netherlands, 15, 265
Blanton, M. R., Bershady, M. A., Abolfathi, B., et al. 2017, AJ, 154, 28
Boeche, C., Chiappini, C., Minchev, I., et al. 2013, A&A, 553, A19
Boubert, D., & Evans, N. W. 2016, ApJL, 825, L6
Boubert, D., Guillochon, J., Hawkins, K., et al. 2018, MNRAS, 479, 2789
Bovy, J. 2015, ApJS, 216, 29
Bowen, I. S., & Vaughan, A. H. J. 1973, ApOpt, 12, 1430
Bressan, A., Marigo, P., Girardi, L., et al. 2012, MNRAS, 427, 127
Brown, A. G. A. 2021, ARA&A, 59, 59
Brown, W. R., Geller, M. J., & Kenyon, S. J. 2014, ApJ, 787, 89
Brown, W. R., Geller, M. J., Kenyon, S. J., & Kurtz, M. J. 2005, ApJL, 622, L33
Brown, W. R., Lattanzi, M. G., Kenyon, S. J., & Geller, M. J. 2018, ApJ, 866, 39
Capuzzo-Dolcetta, R., & Fragione, G. 2015, MNRAS, 454, 2677
Choi, J., Dotter, A., Conroy, C., et al. 2016, ApJ, 823, 102
Cui, X.-Q., Zhao, Y.-H., Chu, Y.-Q., et al. 2012, RAA, 12, 1197
Cunha, K., Smith, V. V., Hasselquist, S., et al. 2017, ApJ, 844, 145
Di Matteo, P., Haywood, M., Lehnert, M. D., et al. 2019, A&A, 632, A4
Dotter, A. 2016, ApJS, 222, 8
Drimmel, R., & Poggio, E. 2018, RNAAS, 2, 210
Eisenstein, D. J., Weinberg, D. H., Agol, E., et al. 2011, AJ, 142, 72
Fernández-Trincado, J. G., Beers, T. C., Minniti, D., et al. 2020, A&A, 643, L4
Freeman, K., & Bland-Hawthorn, J. 2002, ARA&A, 40, 487
Gaia Collaboration, Prusti, T., de Bruijne, J. H. J., et al. 2016, A&A, 595, A1
Gaia Collaboration, Brown, A. G. A., Vallenari, A., et al. 2018, A&A, 616, A1
Gaia Collaboration, Brown, A. G. A., Vallenari, A., et al. 2021, A&A, 649, A1
García Pérez, A. E., Allende Prieto, C., Holtzman, J. A., et al. 2016, AJ, 151, 144
Gnedin, O. Y., Gould, A., Miralda-Escudé, J., & Zentner, A. R. 2005, ApJ, 634, 344
Gravity Collaboration, Abuter, R., Amorim, A., et al. 2018, A&A, 615, L15
Green, G. 2018, JOSS, 3, 695
Gunn, J. E., Siegmund, W. A., Mannery, E. J., et al. 2006, AJ, 131, 2332
Hasselquist, S., Shetrone, M., Cunha, K., et al. 2016, ApJ, 833, 81
Hasselquist, S., Hayes, C. R., Lian, J., et al. 2021, ApJ, 923, 172
Hattori, K., Valluri, M., Bell, E. F., & Roederer, I. U. 2018a, ApJ, 866, 121
Hattori, K., Valluri, M., & Castro, N. 2018b, ApJ, 869, 33
Hawkins, K., Jofré, P., Masseron, T., & Gilmore, G. 2015, MNRAS, 453, 758
Hawkins, K., & Wyse, R. F. G. 2018, MNRAS, 481, 1028
Hayes, C. R., Majewski, S. R., Shetrone, M., et al. 2018, ApJ, 852, 49
Heber, U., Edelmann, H., Napiwotzki, R., Altmann, M., & Scholz, R. D. 2008, A&A, 483, L21
Helmi, A., Babusiaux, C., Koppelman, H. H., et al. 2018, Natur, 563, 85
Herzog-Arbeitman, J., Lisanti, M., & Necib, L. 2018, JCAP, 2018, 052
Hills, J. G. 1988, Natur, 331, 687
Holtzman, J. A., Shetrone, M., Johnson, J. A., et al. 2015, AJ, 150, 148
Irrgang, A., Kreuzer, S., & Heber, U. 2018, A&A, 620, A48
Irrgang, A., Wilcox, B., Tucker, E., & Schiefelbein, L. 2013, A&A, 549, A137
Jönsson, H., Allende Prieto, C., Holtzman, J. A., et al. 2018, AJ, 156, 126
Jönsson, H., Holtzman, J. A., Allende Prieto, C., et al. 2020, AJ, 160, 120
Kobayashi, C., Karakas, A. I., & Lugaro, M. 2020a, ApJ, 900, 179
Kobayashi, C., Leung, S.-C., & Nomoto, K. 2020b, ApJ, 895, 138
Koppelman, H. H., Helmi, A., Massari, D., Price-Whelan, A. M., & Starkenburg, T. K. 2019, A&A, 631, L9
Kreuzer, S., Irrgang, A., & Heber, U. 2020, A&A, 637, A53
Lane, J. M. M., Bovy, J., & Mackereth, J. T. 2022, MNRAS, 510, 5119
Leung, H. W., & Bovy, J. 2019, MNRAS, 489, 2079
Li, Y.-B., Luo, A. L., Lu, Y.-J., et al. 2021, ApJS, 252, 3
Mackereth, J. T., Schiavon, R. P., Pfeffer, J., et al. 2019, MNRAS, 482, 3426
Majewski, S. R., Schiavon, R. P., Frinchaboy, P. M., et al. 2017, AJ, 154, 94
Marchetti, T. 2021, MNRAS, 503, 1374
Marchetti, T., Rossi, E. M., & Brown, A. G. A. 2019, MNRAS, 490, 157
Martell, S. L., Sharma, S., Buder, S., et al. 2017, MNRAS, 465, 3203
McMillan, P. J. 2017, MNRAS, 465, 76
Mészáros, S., Allende Prieto, C., Edvardsson, B., et al. 2012, AJ, 144, 120
Miyamoto, M., & Nagai, R. 1975, PASJ, 27, 533
Monty, S., Venn, K. A., Lane, J. M. M., Lokhorst, D., & Yong, D. 2020, MNRAS, 497, 1236
Morton, T. D. 2015, isochrones: Stellar model grid package, ascl:1503.010
Myeong, G. C., Vasiliev, E., Iorio, G., Evans, N. W., & Belokurov, V. 2019, MNRAS, 488, 1235
Nidever, D. L., Holtzman, J. A., Allende Prieto, C., et al. 2015, AJ, 150, 173
Nissen, P. E., & Schuster, W. J. 2010, A&A, 511, L10
Nomoto, K., Kobayashi, C., & Tominaga, N. 2013, ARA&A, 51, 457
Paxton, B., Bildsten, L., Dotter, A., et al. 2011, ApJS, 192, 3
Paxton, B., Cantiello, M., Arras, P., et al. 2013, ApJS, 208, 4
Paxton, B., Marchant, P., Schwab, J., et al. 2015, ApJS, 220, 15
Pereira, C. B., Jilinski, E., Drake, N. A., et al. 2012, A&A, 543, A58

Piffl, T., Scannapieco, C., Binney, J., et al. 2014, A&A, 562, A91
Poveda, A., Ruiz, J., & Allen, C. 1967, BOTT, 4, 86
Price-Whelan, A. 2018, adrn/pyia v0.2, a Python package for working with data from the Gaia mission, Zenodo, doi:10.5281/zenodo.1228136
Przybilla, N., Fernanda Nieva, M., Heber, U., & Butler, K. 2008, ApJL, 684, L103
Queiroz, A. B. A., Anders, F., Santiago, B. X., et al. 2018, MNRAS, 476, 2556
Queiroz, A. B. A., Anders, F., Chiappini, C., et al. 2020, A&A, 638, A76
Reggiani, H., Ji, A. P., Schlaufman, K. C., et al. 2022, AJ, 163, 252
Riello, M., De Angeli, F., Evans, D. W., et al. 2021, A&A, 649, A3
Rybizki, J., Demleitner, M., Bailer-Jones, C., et al. 2020, PASP, 132, 074501
Rybizki, J., Green, G., Rix, H.-W., et al. 2022, MNRAS, 510, 2597
Santana, F. A., Beaton, R. L., Covey, K. R., et al. 2021, AJ, 162, 303
Schlafly, E. F., & Finkbeiner, D. P. 2011, ApJ, 737, 103
Shen, K. J., Boubert, D., Gänsicke, B. T., et al. 2018, ApJ, 865, 15
Shetrone, M., Bizyaev, D., Lawler, J. E., et al. 2015, ApJS, 221, 24
Shipp, N., Erkal, D., Drlica-Wagner, A., et al. 2021, ApJ, 923, 149
Smith, V. V., Bizyaev, D., Cunha, K., et al. 2021, AJ, 161, 254
Soubiran, C., Jasniewicz, G., Chemin, L., et al. 2018, A&A, 616, A7
Unwin, S. C., Shao, M., Tanner, A. M., et al. 2008, PASP, 120, 38
van der Marel, R. P., & Kallivayalil, N. 2014, ApJ, 781, 121
Wilson, J. C., Hearty, F. R., Skrutskie, M. F., et al. 2019, PASP, 131, 055001
Yoon, J., Beers, T. C., Placco, V. M., et al. 2016, ApJ, 833, 20
Yu, Q., & Madau, P. 2007, MNRAS, 379, 1293
Zasowski, G., Johnson, J. A., Frinchaboy, P. M., et al. 2013, AJ, 146, 81
Zasowski, G., Cohen, R. E., Chojnowski, S. D., et al. 2017, AJ, 154, 198